remote sensing

Article

Simulation of Compact Spaceborne Lidar with High-Repetition-Rate Laser for Cloud and Aerosol Detection under Different Atmospheric Conditions

Jie Ji [1,2,3], Chenbo Xie [1,3,*], Kunming Xing [1,3], Bangxin Wang [1,3], Jianfeng Chen [1,2,3], Liangliang Cheng [4] and Xu Deng [1,2,3]

[1] Key Laboratory of Atmospheric Optics, Anhui Institute of Optics and Fine Mechanics, Hefei Institutes of Physical Science, Chinese Academy of Sciences, Hefei 230031, China
[2] Science Island Branch of Graduate School, University of Science and Technology of China, Hefei 230026, China
[3] Advanced Laser Technology Laboratory of Anhui Province, Hefei 230037, China
[4] Anhui Province Key Laboratory of Simulation and Design for Electronic Information System, Hefei Normal University, Hefei 230601, China
* Correspondence: cbxie@aiofm.ac.cn

Abstract: To provide references for the design of the lab's upcoming prototype of the compact spaceborne lidar with a high-repetition-rate laser (CSLHRL), in this paper, the detection signal of spaceborne lidar was simulated by the measured signal of ground-based lidar, and then, the detection capability of spaceborne lidar under different atmospheric conditions was evaluated by means of the signal-to-noise ratio (SNR), volume depolarization ratio (VDR) and attenuated color ratio (ACR). Firstly, the Fernald method was used to invert the optical parameters of cloud and aerosol with the measured signal of ground-based lidar. Secondly, the effective signal of the spaceborne lidar was simulated according to the known atmospheric optical parameters and the parameters of the spaceborne lidar system. Finally, by changing the cumulative laser pulse number and atmospheric conditions, a simulation was carried out to further evaluate the detection performance of the spaceborne lidar, and some suggestions for the development of the system are given. The experimental results showed that the cloud layer and aerosol layer with an extinction coefficient above 0.3 km^{-1} could be easily obtained when the laser cumulative pulse number was 1000 and the vertical resolution was 15 m at night; the identification of moderate pollution aerosols and thick clouds could be easily identified in the daytime when the laser cumulative pulse number was 10,000 and the vertical resolution was 120 m.

Keywords: spaceborne lidar; active remote sensing; cloud and aerosol; extinction coefficient

Citation: Ji, J.; Xie, C.; Xing, K.; Wang, B.; Chen, J.; Cheng, L.; Deng, X. Simulation of Compact Spaceborne Lidar with High-Repetition-Rate Laser for Cloud and Aerosol Detection under Different Atmospheric Conditions. *Remote Sens.* **2023**, *15*, 3046. https://doi.org/10.3390/rs15123046

Academic Editor: Michael Obland

Received: 15 May 2023
Revised: 7 June 2023
Accepted: 8 June 2023
Published: 10 June 2023

1. Introduction

Clouds and aerosols play a very important role in Earth's climate change. On the one hand, cloud particles and aerosol particles can change the radiation balance of Earth's atmosphere system by absorbing and scattering sunlight. On the other hand, aerosol particles can directly affect the formation of clouds and precipitation as condensation nuclei [1–5]. Therefore, it is of positive significance to study the spatial distribution and change process of clouds and aerosols for improving the precision of weather forecast and predicting global climate change [6–9]. In order to realize the real-time dynamic monitoring of global clouds and aerosols, spaceborne lidar remote sensing has become a hotspot of environmental surveillance research [10–13]. However, due to the limitation of the orbit and operation mechanism, the measurement data of a single spaceborne lidar cannot accurately describe atmospheric conditions, so it is necessary to adopt other technical means and build the lidar surveillance network to improve the precision of detection. The traditional spaceborne lidar systems usually adopted the detection technology route of a high-energy, low-repetition-rate pulsed laser and a receiving telescope with a large diameter. They usually adopted a laser with a single-pulse energy of hundreds of mJ and a repetition rate of tens of Hz, as well as a receiving optical telescope with a diameter of more than 1 m, such as the Cloud–Aerosol Lidar and Infrared Pathfinder Satellite Observation (CALIPSO), Atmospheric Dynamics Mission (ADM), and Lidar In-Space Technology Experiment (LITE). High-powered lasers and large aperture telescopes allow them to have a high signal-to-noise ratio, even during the daytime, when the solar background radiation is strong. However, high-power lasers are large and require water cooling. The above characteristics make the volume and mass of high-power spaceborne lidar very large and require a large space load. For example, LITE was fixed on the space shuttle, while CALIPSO needed a specialized satellite to carry it, making the development of high-power spaceborne lidar a long and expensive process [14–20]. At the same time, due to the repetition rate of the laser being tens of Hz, its atmospheric refined measurement ability in specific application scenarios such as aerosols and clouds is insufficient. For example, CALIPSO has a distance of 200 km between orbits, while obtaining an effective vertical extinction profile requires data accumulation with a horizontal resolution of 40 km and a vertical resolution of 120 m, making it difficult to obtain refined atmospheric measurement data.

A new spaceborne lidar atmospheric detection technique based on a high-repetition-rate laser and single-photon-counting technique represented by the Cloud-photon Transport System (CATS) was applied to realize the aerosol detection target with a small size, low cost, and refined, which further meet the requirement of spaceborne lidar networking. On the premise of a sufficient signal-to-noise ratio of single-pulse energy, the signal-to-noise ratio can be improved by increasing the cumulative pulse number, which can be achieved with a high-repetition-frequency laser. They often use detectors with photon counting mode, which are more sensitive to detection, but are also more susceptible to solar background radiation during daytime. Low-power spaceborne lidars have low volume, mass, and power consumption and do not require a special space load, which makes it have high flexibility. At the same time, low-power spaceborne lidar tends to be commercialized and low cost and has a short development cycle. A small team can rapidly and cost-effectively design, build, test, and deploy a space lidar capable of hundreds and thousands of hours of operation [21–25].

In summary, our team plans to develop a compact spaceborne lidar system with a high-repetition-rate laser for the preliminary identification of clouds and aerosols in polluted atmosphere. Table 1 shows the comparison of the main parameters between CSLHRL and current spaceborne lidars.

Table 1. Comparison of the main parameters between CSLHRL and current spaceborne lidars.

	CALIPSO	**ADM**	**LITE**	**CATS**	**CSLHRL**
Technical means	High-laser-energy atmospheric detection lidar	High-laser-energy Doppler lidar	High-laser-energy atmospheric detection lidar	Lo- energy single-photon detection lidar	Low-energy single-photon detection lidar
Laser	100 mJ/20.25 Hz	150 mJ/100 Hz	486 mJ/10 Hz/1064 nm 460 mJ/10 Hz/532 nm 196 mJ/10 Hz/355 nm	1 mJ/5 kHz	3 mJ/1 kHz/532 nm 6 mJ/1 k Hz/1064 nm
Diameter of the telescope (cm)	100	150	94.6	60	40
Detector (nm)	PMT (532) APD (1064)	ACCD	PMT (355 532) APD (1064)	APD (532) APD (1064)	APD (532) APD (1064)
Acquisition card	A/D	--	A/D	Single photon counting	Single photon counting
Mass (kg)	587 (156)	1366 (460)	2000	494	70–90
Volume (m × m × m)	1.80 × 1.50 × 1.31	1.74 × 1.9 × 2.0	--	--	0.8 × 0.7 × 0.7
Power consumption (W)	560	840	3000	--	250
Orbital altitude (km)	705	408	250	405	600

Before the development of a lidar system, it is necessary to carry out the corresponding simulation according to the requirements of system design. The results of simulation can verify the correctness and feasibility of the system design and provide optimization suggestions for the design scheme [26]. At the same time, the simulation results can provide initial values for the subsequent inversion of atmospheric parameters. By optimizing the parameters, the simulation results can be as close to the actual results as possible, so as to achieve high-precision inversion. In 1989, Sasano et al. found that multi-wavelength lidar had the potential to distinguish several aerosol types such as marine, continental, stratospheric, and desert aerosols based on the wavelength dependence of aerosol backscattering coefficients. By comparing the measured aerosol data with the simulation results, they found that there was a large difference between them and put forward a reasonable guess about the result [27]. In 1999, Frehlic et al. used computer simulations of raw data and statistical descriptions of the resulting velocity estimates to evaluate the performance of space-based lidar and used coprocessing of multiple shots for a fixed lidar beam geometry to improve the performance of the lidar based on the simulation [28]. In 2002, Liu and Sugimoto conducted a simulation study on spaceborne lidar photomultiplier tubes and found that the electron distribution of the lidar echo signal amplified by photomultiplier tubes meets Neyman Type A. On this basis, the echo signal of spaceborne lidar was simulated, and the process of cloud detection by the threshold method was demonstrated [29]. In 2013, Filipitsch et al. proposed to use the Monte-Carlo-based exact lidar retrieval algorithm (ARLEM) to simulate spaceborne high-spectral-resolution lidar measurement (HSRL) in order to reduce the influence of multiple scattering on spaceborne lidar detection and added real signal and instrument noise. It was found that the main source of uncertainty of inversion was the content of ice water in cirrus cloud [30]. In 2015, Boquet et al. proposed a new method for predicting the effective detection distance of coherent wind Doppler lidar (CWDL), which combined the measured aerosol optical parameters and simulated instrument parameters to build a prediction model and compared the predicted results with the actual ones. The results showed that the method was applicable to any target area where atmospheric data can be obtained and provided a method for the operation of the diagnostic instrument, which provided a reference for the design of a lidar system in the future [31]. In the same year, Reverdy et al. evaluated the detection performance of Atmospheric Lidar (ATLID) carried by the Earth Care satellite by constructing a COSP/ATLID simulator. The results showed that, under the premise of considering the major differences between ATLID and CALIOP, the difference in cloud cover measured by COSP/ATLID and COSP/CALIPSO was less than 1% under night conditions [32].

In the optimization scheme design of the system, it is necessary to conduct quantitative research and simulation calculation on the correlation between on-orbit detection of atmospheric aerosol and cloud characteristics and lidar system parameters, so as to give the best system parameters and possible performance indicators. In this paper, atmospheric optical parameters measured on the ground were used to simulate the spaceborne lidar signal under different conditions. The atmospheric conditions, the cumulative number of laser pulses, and the spatial resolution were considered comprehensively. The experimental results can provide a preliminary reference for the subsequent development of a spaceborne lidar system.

2. Simulation Process

The input values of the optical parameters of atmospheric aerosol and cloud particles have a great influence on the accuracy of the simulation results. On the one hand, as the spaceborne lidar parameters are to be measured, their numerical accuracy will determine the simulation results; on the other hand, due to the complex sources of atmospheric aerosol and cloud particles, their vertical and spatial distributions cannot be accurately described by models. Therefore, only the optical parameter data of atmospheric aerosol and cloud particles measured by ground-based lidar can be used for spaceborne lidar simulation.

In this section, the simulation process of the spaceborne lidar signal based on the ground-based lidar measured signal is analyzed from the lidar equation, the influence of background signal and noise on the simulation results is analyzed, and the suggestions for the selection of lidar system parameters are given. The simulation process is shown in Figure 1.

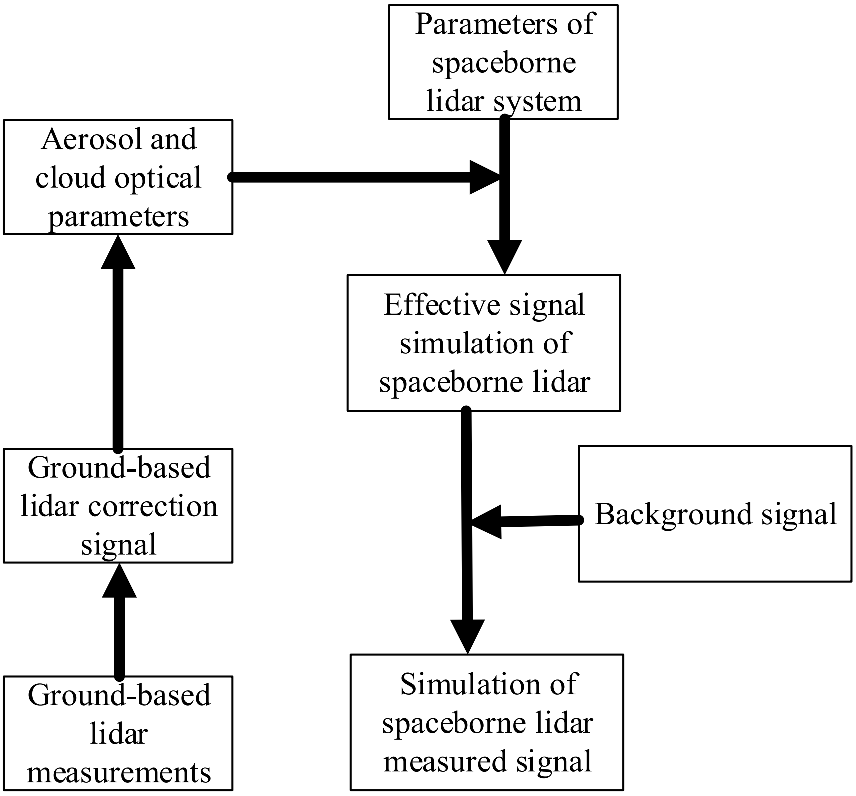

Figure 1. Simulation flow of spaceborne lidar signal based on ground-based lidar measurement data.

The specific steps of simulation are as follows

(1) Based on the measurement data of the ground-based lidar, the correction signal of the ground-based lidar system was obtained by background deduction, distance correction, geometric factor correction, and noise smoothing data in sequence;
(2) The backscattering ratio, extinction, and backscattering coefficients of atmospheric aerosol and cloud particles under different atmospheric conditions were obtained by the aerosol and cloud inversion algorithm;
(3) Based on spaceborne lidar system parameters, ground-based lidar inversion of aerosol and cloud particles' optical parameters, and the spaceborne lidar signal simulation algorithm, the spaceborne lidar atmospheric echo effective signal was simulated;
(4) Through the spaceborne lidar system parameters and atmospheric background data, the noise signal of the simulation system was simulated and superimposed on the effective signal, and finally, the actual measurement signals of the spaceborne lidar with background and its signal-to-noise ratio (SNR) were obtained.

2.1. Simulation of the Effective Signal of Spaceborne Lidar Based on Ground-Measured Signal

2.1.1. Inversion of Optical Parameters of Ground-Based Lidar

When lidar is used for atmospheric detection, taking the Mie scattering lidar as an example, the atmospheric backscatter echo signal received by it can be expressed as [33]:

$$P(z) = Cz^{-2}[\beta_a(z) + \beta_m(z)] \exp\left\{-2\int_0^z [\alpha_a(z') + \alpha_m(z')]dz'\right\} \tag{1}$$

where *P(z)* is the echo power (*W*) received by the lidar from the distance *z*, *C* is a system constant; $\beta_a(z)$ and $\beta_m(z)$ are the backscattering coefficients of aerosols and molecules at a distance of *z*, respectively, and $\alpha_a(z')$ and $\alpha_m(z')$ are the extinction coefficients of aerosols and molecules at the distance *z*, respectively [33].

$$\alpha_a(z) = \beta_z(z) \cdot S_1 \tag{2}$$

$$\alpha_m(z) = \beta_m(z) \cdot S_2 \tag{3}$$

$$R_b(z_c) = [\beta_m(z_c) + \beta_a(z_c)]/\beta_m(z_c) \tag{4}$$

S_1 is the aerosol extinction backscattering ratio, whose value is affected by the aerosol scale spectrum and refractive index, usually between 10 sr and 100 sr. In the Fernald method, assuming that S_1 is a constant that does not vary with height, S_1 = 50 is preferred in the tropospheric and stratospheric background periods [33]. The molecular-extinction-to-backscattering ratio of S_2 is usually taken as $8\pi/3$. z_c is the height of the calibrated layer, and the backscattering ratio $R_b(z_c)$ at this height is assumed to be known.

According to the U.S. Standard Atmosphere model, the molecular backscattering coefficient can be determined by the following equation:

$$\beta_M(z, \lambda) = 1.1706 \times 10^{-23} \cdot \frac{273}{T(z)} \cdot \frac{P_a(z)}{1013} \cdot \left(\frac{10^7}{\lambda}\right)^{4.0117} \tag{5}$$

$T(z)$ is the atmospheric temperature (K) at a distance of z; $P_a(z)$ is the atmospheric pressure at a distance of z (hPa); λ is the wavelength of the laser. Atmospheric temperature and pressure profiles are given by the mode.

Equations (2)–(5) are substituted into Equation (1) to calculate the extinction coefficient of aerosol:

$$\begin{gathered}\alpha_a(z) = -\tfrac{S_1}{S_2}\alpha_m(z) + \\ \frac{X(z)\exp[2(\frac{S_1}{S_2}-1)\int_z^{z_c}\alpha_m(z')\mathrm{d}z']}{\frac{X(z_c)}{\alpha_a(z_c)+\frac{S_1}{S_2}\alpha_m(z_c)} + 2\int_z^{z_c} X(z')\exp[2(\frac{S_1}{S_2}-1)\int_z^{z_c}\alpha_m(z'')\mathrm{d}z'']\mathrm{d}z'}\end{gathered} \tag{6}$$

$$\begin{gathered}\alpha_a(z) = -\tfrac{S_1}{S_2}\alpha_m(z) + \\ \frac{X(z)\exp[-2(\frac{S_1}{S_2}-1)\int_{z_c}^{z}\alpha_m(z')\mathrm{d}z']}{\frac{X(z_c)}{\alpha_a(z_c)+\frac{S_1}{S_2}\alpha_m(z_c)} - 2\int_{z_c}^{z} X(z')\exp[2(-\frac{S_1}{S_2}-1)\int_{z_c}^{z}\alpha_m(z'')\mathrm{d}z'']\mathrm{d}z'}\end{gathered} \tag{7}$$

Equation (6) is the extinction coefficient of atmospheric aerosol when the height is below z_c, which takes the form of a backward integral. Equation (7) is the extinction coefficient of atmospheric aerosol when the height is above z_c, and it takes the form of a forward integral. $X(z) = P(z)z^2$ is the distance-squared signal (known as the range-corrected signal (RCS)).

2.1.2. Simulation of Effective Signals of Spaceborne Lidar

The laser transmission position of spaceborne lidar is different from that of ground-based lidar. As shown in Figure 2, the height of the detected target from the ground is z, and the orbital height of the satellite is 600 km. The expression equation of spaceborne lidar needs to be transformed into the form of Equation (8):

$$\begin{gathered}P(z) = C(600-z)^{-2}[\beta_a(600-z) + \beta_m(600-z)] \\ \exp\left\{-2\int_{600-z}^{600}[\alpha_a(600-z') + \alpha_m(600-z')]dz'\right\}\end{gathered} \tag{8}$$

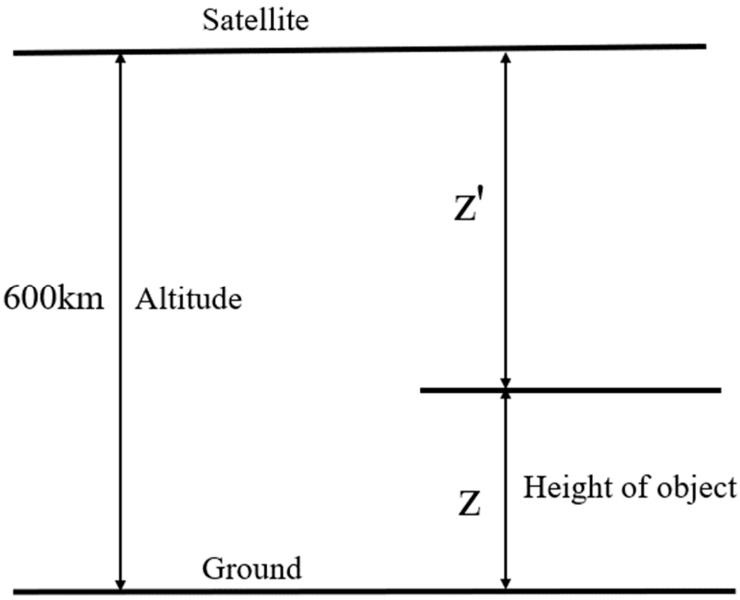

Figure 2. Spaceborne lidar detection diagram.

Converted to photon number, the atmospheric backscattering echo signal received by lidar corresponding to each laser pulse can be written as [34]:

$$\begin{cases} Ns(z) = P(600-z)(\frac{\eta\lambda}{hc})\Delta t = \frac{cE_0 Y(600-z) Ar \beta(600-z) T^2(600-z) TtTr}{2(600-z)^2}(\frac{\eta\lambda}{hc})\Delta t; \\ T(z) = \exp(-\int\limits_{600-z}^{600} \alpha(600-z')dz'); \\ \Delta t = \frac{2\Delta z}{c}; \\ \alpha(600-z) = \alpha_a(600-z) + \alpha_m(600-z); \beta(600-z) = \beta_a(600-z) + \beta_m(600-z) \end{cases} \quad (9)$$

where $Ns(z)$ is the photon number of the atmospheric backscattering echo signal at height z from the satellite; P(600-z) is the atmospheric backscattering echo power (W) at height z from the ground(km); η is photodetector quantum efficiency; λ is the laser transmission wavelength (nm); $h = 6.6262 \times 10^{-34}$ is Planck's constant (J·s); $c = 3.0 \times 10^8$ is the speed of light in vacuum (m/s); Δt is the time resolution of lidar detection (s); E_0 is the monopulse energy of laser transmission (J); Y(600-z) is the overlap factor at height z from the ground; Ar is the receiving area of the telescope (m^2); β(600-z) is the atmosphere backscattering coefficient (sr^{-1} km^{-1}), and it includes the contribution of aerosol particles and gas molecules; $T(z)$ is the atmospheric transmittance from the lidar to altitude z; T_t is the transmittance of the transmitting optical unit; T_r is the transmittance of the receiving optical unit; Δz is the range resolution (km) detected by the lidar.

In Equation (9), α_a(600-z), α_m (600-z), β_a(600-z), and β_m(600-z) can be obtained by the calculation of Equations (2)–(7) (due to the limited detection height of ground-based lidar and low aerosol content in the upper air, α_a and α_m above 30 km were considered to be 0 km^{-1}); because the atmospheric optical parameters in the overlap region of spaceborne lidar were not the focus of study, Y(600-z) was considered to be 1 in the simulation. Other system parameters should be selected according to the actual design requirements of CSLHRL.

The schematic diagram of CSLHRL is shown in Figure 3. The main units of the system include the laser transmitting unit, optical receiving unit, signal reception and system control unit, and signal detection unit. In the laser transmitting unit, two lasers were used to emit 532 nm and 1064 nm wavelengths, respectively, which are reflected into the atmosphere through the self-regulating mirror after beam expansion. In the optical receiving unit, a Cassegreen telescope with a 400 mm aperture and 2000 mm focal length was used. The receiving field of view was 0.2 mrad through a 0.3 mm aperture without considering the external load. In the signal detection unit, the background suppression of the 532 nm and 1064 nm channels is performed by using a Fabry–Perot Interferometer (F-P). The detection unit and the acquisition unit adopt the avalanche photo diode (apd) based on the weak signal detection technology of photon counting to realize the highly sensitive detection of atmospheric backwave optical signals in a large dynamic range.

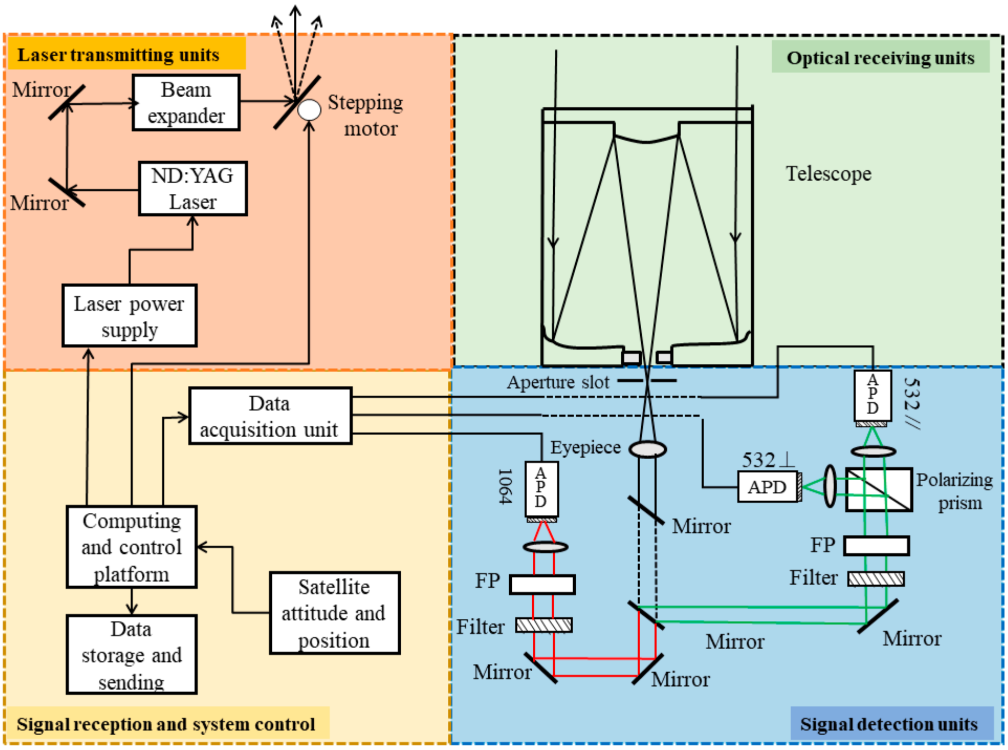

Figure 3. Schematic diagram of CSLHRL.

Based on the design parameters and measurement parameters of the spaceborne lidar system, the on-orbit measurement performance of the spaceborne lidar system was simulated. Table 2 shows the input values of the system parameters and measurement parameters in the spaceborne lidar simulation. The selection of the parameters in Table 2 shows that we comprehensively considered the design requirements of the lidar system, such as the volume, mass, power, detection performance, etc. On this basis, we selected the parameters in the table and show the simulation results under this condition in the paper.

Table 2. Input values of system parameters and measurement parameters in spaceborne lidar simulation.

Lidar Unit	System Parameters	The Input Value of the Simulation
Laser transmitting units	Single-pulse laser energy	3 mJ@532 nm 6 mJ@1064 nm
	Laser transmission frequency	1000 Hz
	Transmission optical efficiency	95%
Optical receiving units	Telescope receiving aperture	400 mm
	Receiving field angle	0.2 mrad
	Receiving optical efficiency	0.4
	Filter bandwidth	0.3 nm

Table 2. *Cont.*

Lidar Unit	System Parameters	The Input Value of the Simulation
Signal detection units	Detection efficiency	60%@532 nm 5%@1064 nm
	Dark count rate	100 Hz
	Extinction ratio of polarizing prism	3000:1
Data receiving units	Sampling resolution	15 m (100 ns)
	Sampling depth	40,000
Satellite load units	Orbital altitude	600 km
	Sky background radiation	0.2@532 nm(W·m^{-2}·sr^{-1}·nm^{-1}) 0.08@1064 nm(W·m^{-2}·sr^{-1}·nm^{-1})
	Vertical resolution	15 m~120 m (vertical resolution)
	Horizontal resolution	1 s~10 s (7~70 km horizontal resolution)

2.2. Simulation of Background Signal and Noise of Spaceborne Lidar

The optical signals received by the spaceborne lidar system not only include backscattering light signals generated by the interaction between the laser and air molecules, aerosol, and cloud particles, but also include atmospheric background radiation light signals, as well as the noise signals of the detector itself.

The sky background light signals corresponding to each pulse received by the spaceborne lidar system are shown as follows [35]:

$$Nb = \frac{\eta\lambda}{hc} Pb\pi(\theta/2)^2 d_{wl} A_r T_r \Delta t \tag{10}$$

where Nb is the number of sky background photons received by each pulse; Pb is the sky background radiation intensity (W·m^{-2}·sr^{-1}·nm^{-1}), and for a 532 nm wavelength, it is generally believed Pb = 0.2 W·m^{-2}·sr^{-1}·nm^{-1} in the daytime; θ is the viewing angle of the telescope (mrad); $d_{\omega 1}$ is filter bandwidth (nm); A_{r} is the receiving area of the telescope (m^2); T_{r} is the optical transmittance of the lidar receiving optical unit; Δt is the time resolution (s) of the lidar.

According to Equation (10), factors affecting the intensity of the sky background radiation signal received by the lidar are also composed of three parts.

The first part is the system parameters, which mainly include the receiving area of the telescope, the optical transmittance of the receiving optical unit, the receiving field angle, the filter bandwidth, and the detection efficiency. Considering the requirement of lidar signal intensity measurement, only the receiving field angle and filter bandwidth are the main factors to limit the background signal.

The second part is the atmospheric parameter, which is mainly related to the intensity of sky background radiation.

The third part is the measurement parameters, including the measurement time, which is related to the vertical resolution and horizontal resolution of the lidar.

Table 3 shows the analysis of the main factors affecting the background intensity measured by the spaceborne lidar. It can be seen from the table that, among the atmospheric parameters, the intensity of the sky background radiation had the highest effect ratio on the background signal measured by the spaceborne lidar, with a difference of 4 to 5 orders of magnitude. At the same time, considering the demand of the measured signal of the lidar, the only factors that can reduce the intensity of the background signal are the receiving field angle and filter bandwidth.

Table 3. Analysis of influence factors of background signal measured by spaceborne lidar.

Influence Categories	Influence Factors	Parameters Range	Influence Ratio	Remarks
System parameters	Receiving area	0.125~0.785 (m^2)	6.3	0.4~1 m caliber
	Optical transmittance	10%~50%	5	--
	Receiving field Angle	0.1~0.5 (mrad)	5	--
	Filter bandwidth	0.01~0.3 (nm)	30	--
	Detection efficiency	4%~80%	20	--
Atmospheric parameters	Sky background radiation intensity	0~0.2@532 nm/0.08@1064 nm ($W \cdot m^{-2} \cdot sr^{-1} \cdot nm^{-1}$)	>10,000	night~day
Measurement parameters	Spatial resolution	15~300 (m)	20	--
	Time resolution	1~20 (s)	20	7~150 km

In the mode of photon counting of the detector, the simulated signal noise mainly includes the signal scattering noise caused by echo photons, the background light scattering noise caused by sky background photons, and the detection dark noise, and the above noise accords with the Poisson distribution. Noise intensity can be expressed as follows [35]:

$$Noise = \sqrt{\frac{Ns(z) + Nb + Nd}{M}} \tag{11}$$

Noise is the intensity of noise; Ns (z) is the number of echo photons at a height of z from the ground; Nb is the number of sky background photons; Nd is the detector dark count (10–5 per pulse); M is the number of laser pulses. By combining Equations (9)–(11), simulated spaceborne lidar signals can be obtained.

2.3. Simulation of the Signal-to-Noise Ratio of Spaceborne Lidar Signal

The signal-to-noise ratio (SNR) of spaceborne lidar signal is an important index to characterize the detection performance of the system and an important parameter to control the quality of data inversion. The equation for calculating the *SNR* of the lidar measurement signal is as follows [35]:

$$SNR(z) = \frac{Ns(z)}{\sqrt{Ns(z) + Nb + Nd}} \times \sqrt{M} \tag{12}$$

where $SNR(z)$ is the signal-to-noise ratio of the lidar measured signal; $Ns(z)$ is the photon number of the measured signal under the lidar monopulse condition; Nb is the number of sky background photons measured under the lidar monopulse condition; Nd is the dark count of the detector itself under the lidar monopulse condition, generally ranging from 100 to 1000 s^{-1}; M is the cumulative pulse number measured by the lidar.

From the simulation Equation (12), it can be seen that, by increasing the photon number $Ns(z)$ of the lidar measurement signal under the monopulse condition, reducing the sky background photon number Nb and detector dark count Nd, the SNR of spaceborne lidar can be improved. At the same time, increasing the cumulative time of lidar measurement (which will reduce the temporal and spatial resolution) can also improve the SNR of the spaceborne lidar.

2.4. Simulation of the VDR and ACR

The volume depolarization ratio (VDR) of aerosol particles can be calculated by Equation (13) [36].

$$\delta_{VDR}(z,\lambda) = \frac{\beta_s(z,\lambda)}{\beta_p(z,\lambda)} = k_{VDR}(\lambda)\frac{P_{rs}(z,\lambda)}{P_{rp}(z,\lambda)} \tag{13}$$

where the subscripts p and s represent two directions, which are parallel and perpendicular to the polarization direction of the emitted laser, respectively. β_p (z, λ) and β_s (z, λ) represent the parallel polarization component and perpendicular polarization component ($\mathrm{km}^{-1}\mathrm{sr}^{-1}$) of the atmospheric backscattering coefficient at altitude z, respectively. K_{VDR}(λ) = k_p (λ)/k_s (λ) is the gain constant ratio of the two channels. It includes the depolarization effect of the lidar system and the different detection efficiency of two channels, which can be measured by the unpolarized light source method, air molecule method, and 1/2 wave plate method [37]. In this way, the vertical distribution profiles of the atmospheric depolarization ratio δ_{VDR} (z, λ) can be obtained by analyzing the parallel polarization component P_{rp} (z, λ), the perpendicular polarization component P_{rs} (z, λ), and the gain constant ratio k_{VDR} (λ) of the atmospheric backscattering echo power received by the polarization lidar with Equation (13). Since the depolarization ratio of air molecules in the atmosphere is very small, only 0.0297 [38], the atmospheric depolarization ratio δ_{VDR} (z, λ) detected by lidar mainly comes from the contribution of non-spherical particles. Thus, aerosols can be roughly classified by the extinction coefficient and depolarization ratio.

The attenuated color ratio (ACR) of atmospheric aerosol is obtained by the calibrated ratio between the backscatter coefficient of the 1064 nm channel and the backscatter coefficient of the 532 nm channel measured by the lidar. Its calculation formula is as follows:

$$\delta_{ACR}(z) = k_{ACR}\frac{P_{1064}(z)}{P_{532}(z)} \tag{14}$$

Among them, δ_{ACR}(z) is the attenuated color ratio; k_{ACR} is the calibration coefficient at a distance of z; $P_{1064}(z)$ and $P_{532}(z)$ represent the echo power of the 1064 nm and 532 nm channels at a distance of z.

The attenuated color ratio ACR represents the particle size information of aerosol particles, whose value is proportional to the diameter of the particle [39].

3. Simulation Results

The ground-based lidar for atmospheric parameter measurement is the 532 nm single-channel Mie scattering lidar developed by the Chinese Academy of Sciences (the laser frequency is 1 kHz; the overlap height is 250 m; the diameter of the telescope is 450 mm). Since the ground-based lidar does not have polarization channels and the 1064 nm channel, the detection channels of the spaceborne lidar to be simulated include the parallel polarization channel, perpendicular polarization channel, and 1064 nm channel. We assumed that the simulated signal of the spaceborne lidar obtained from Equation (8) is the total 532 nm signal P_{532} and used this to simulate the values of the other three channels, where:

$$\begin{aligned} P_{532}(z) &= P_{rs}(z) + P_{rp}(z) \\ P_{rs}(z) &= P_{532}(z) - P_{rp}(z) \end{aligned} \tag{15}$$

In the process of the inversion of the extinction coefficient with the ground-based lidar, the threshold method was used to determine the spatial distribution of cloud and aerosol near the surface. Based on the spatial distribution information of aerosol and cloud, the VDR of near-surface aerosol was set as 0.2, the VDR of clouds was 0.5, and the VDR of molecules was 0.03 [38], which is the simulated input value of the VDR (assuming that the total 532 nm signal is 1, then according to the description in the manuscript, 532 nm P is 5/6 in the cloud part, and 532 nm S is 1/6 (VDR = 0.5); in the aerosol part, 532 nm P is

2/3532 nm and S is 1/3 (VDR = 0.2)). Set the gain constant ratio k_{VDR} as 1, and substitute Equation (15) into Equation (13), then the simulated signal of parallel polarization channel P_{rp} and perpendicular polarization channel P_{rs} can be obtained, respectively. By adding background radiation and noise to P_{rp} and P_{rs}, the simulated polarization signals P_{rp}' and P_{rs}' with noise and background of the spaceborne lidar can be obtained. By substituting P_{rp}' and P_{rs}' into Equation (13), the simulated VDR of the spaceborne lidar can be obtained, which is the simulated VDR. The extinction coefficients of aerosol with 532 nm retrieved by the ground-based lidar were obtained. According to the spatial distribution information of aerosol and cloud, α_{532} in the aerosol region was multiplied by $(1064/532)^{-1}$ as the simulated aerosol extinction coefficient of the 1064 nm channel. α_{532} in the cloud region was multiplied by $(1064/532)^{-0}$, and the molecular extinction coefficient can be calculated according to Equation (5).

By substituting the above atmospheric parameters and the system parameters in Table 2 into Equation (8), the simulated signal P_{1064}' of the spaceborne lidar can be obtained; by substituting P_{1064} and P_{532} into Equation (14) and setting the calibration coefficient k_{ACR} = 1, the simulated input value of the ACR can be obtained.

By adding background radiation and noise to P_{1064} and P_{532}, the simulated signals P_{1064}' and P_{532}' with noise and background of the spaceborne lidar can be obtained. By substituting P_{1064}' and P_{532}' into Equation (14), the simulated ACR of the spaceborne lidar can be obtained.

In this section, the optical parameters of atmospheric aerosol and cloud particles with two wavelengths of 532 nm and 1064 nm were obtained by ground-based lidar inversion under three typical atmospheric conditions: heavy-pollution low-cloud atmosphere, moderate-pollution high-cloud atmosphere, and clean and cloudy atmosphere. Combined with the input values of the system parameters and measurement parameters given in Table 1 and the simulation process in Figure 1, the simulated signal and SNR of the spaceborne lidar with were analyzed.

3.1. Simulation of Heavy-Pollution Low-Cloud Atmosphere

Figure 4a shows the aerosol extinction coefficient inversed from the ground-based 532 nm Mie-scattered lidar signal during a heavily polluted weather event in Hefei, China, on 20 January 2022. Due to the strong attenuation of the optical parameters of near-surface heavy pollution aerosol and cloud particles, the lidar echo signal above 3 km was very weak. Figure 4b shows the aerosol extinction coefficient of 1064 nm obtained by simulation and inversion based on the measured signal of the 532 nm wavelength. Due to the longer wavelength, the aerosol extinction coefficient was slightly smaller than that of 532 nm. During 14:00 p.m.~23:00 p.m., there was a layer of high-concentration aerosol near the ground, the corresponding extinction coefficient was above 1 km^{-1}, and the visibility was below 4 km.

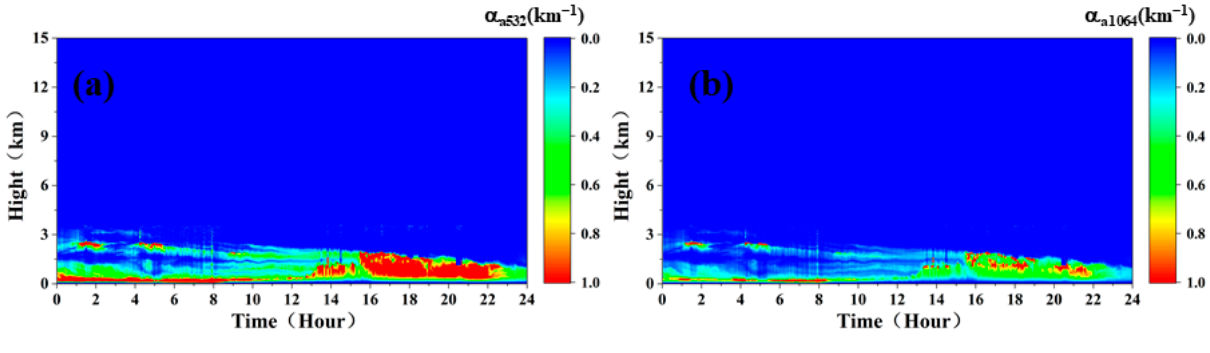

Figure 4. Aerosol extinction coefficient at 532 nm (**a**) and 1064 nm (**b**) wavelengths. (532 nm is from ground-based measurement, and 1064 nm is simulated for ground-based.)

To show the size of the aerosol extinction coefficient more clearly, we chose the extinction coefficient profile at 16:00 p.m., when the pollution was severe, as shown in Figure 5. It can be seen from the figure that the extinction coefficient of the aerosol at 532 nm at that time was near 1 km^{-1}, and even exceeded 3 km^{-1} at 1.7 km. Due to the large aerosol concentration near the ground, the SNR above 1.8 km was poor, and effective data cannot be obtained.

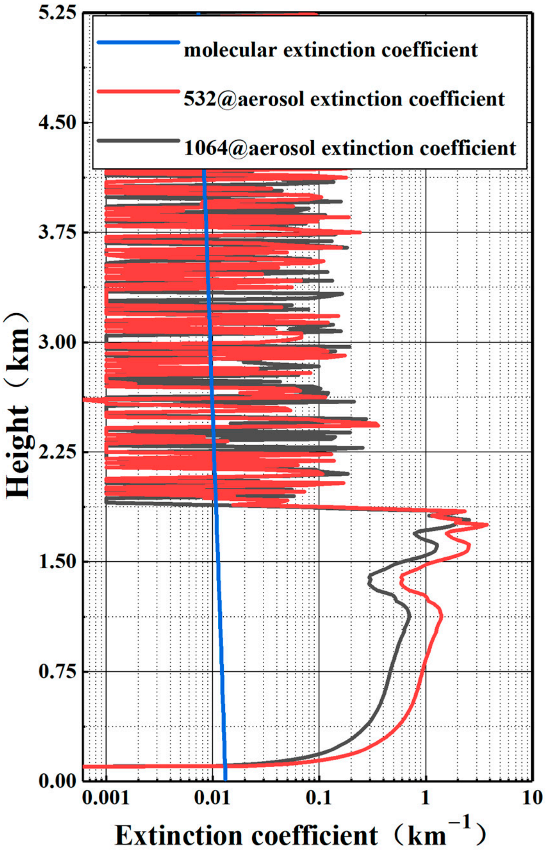

Figure 5. Atmospheric extinction coefficient at 16:00 p.m. (532 nm is from ground-based measurement, and 1064 nm is simulated for ground-based.)

3.1.1. Observation Model at Night

In the night heavy-pollution observation mode, the vertical resolution of the spaceborne lidar was set as 15 m, and the cumulative pulse number was set as 1000 (minimum resolution obtained according to the development plan in Table 2). The extinction coefficients and backscattering coefficients of the aerosols at 532 nm and 1064 nm, the systematic constants in Table 2, and the extinction coefficients and backscattering coefficients of molecules calculated by Equation (5) were substituted into Equation (8) to obtain the simulated signals of their respective channels of spaceborne lidar. The simulated signals of the 532 P, 532 S, and 1064 channels of the spaceborne lidar are shown in Figure 6a–c, respectively (assuming that the sky background radiation intensity is a constant Pb = 0 W·m^{-2}·sr^{-1}·nm^{-1}, which does not change with time).

It can be seen from the simulation results at night that, in the atmospheric boundary layer under heavy-pollution atmospheric conditions, 10~20 photons can be measured in the 532 nm P channel, 5~15 photons can be measured in the 532 nm S channel, and 5~15 photons can be measured in the 1064 nm channel with 1000 laser pulses at 532 nm and 1064 nm.

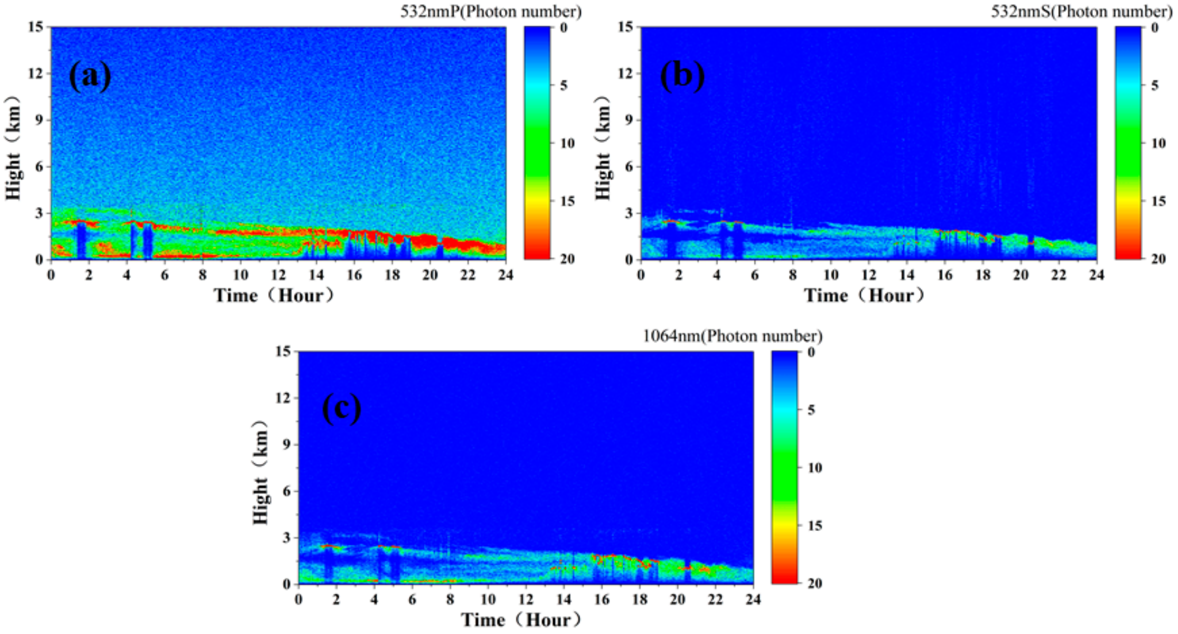

Figure 6. The simulated signal intensity of 532 P (**a**), 532 S (**b**), and 1064 (**c**) channels of spaceborne lidar.

As can be seen from the simulation results of the spaceborne lidar at night in Figure 7, in the atmospheric boundary layer under the condition of heavy pollution, the SNR of the measured signals of the 532 nm P channel was about above 5, and those of the measured signals of 532 nm S and 1064 nm channel were between 2 and 5. The SNR of the measured signals in the atmospheric boundary layer was obviously higher than that above the boundary layer.

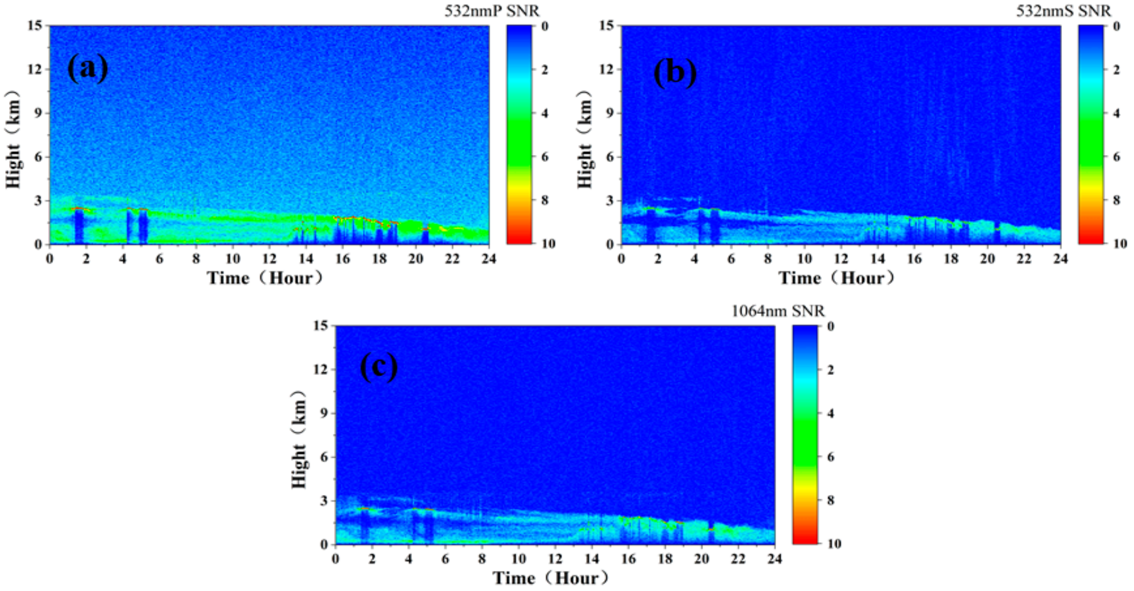

Figure 7. The simulated SNR of 532 P (**a**), 532 S (**b**), and 1064 (**c**) channels at night of spaceborne lidar.

Figure 8 shows the SNR profile at 16:00 p.m. It can be found that the simulated spaceborne lidar signal cannot be received due to the high-concentration pollution aerosol at 0.8–1.6 km, resulting in a poor SNR below 0.8 km. At the altitude of 0.8 km−1.6 km, the aerosol concentration was high, and the SNR of 532 nm P was more than 3, and some altitudes even exceeded 10. In addition, due to the influence of energy and wavelength, the SNRs of the 532 nm and 1064 nm signals were smaller than the SNR of 532 nm P signals.

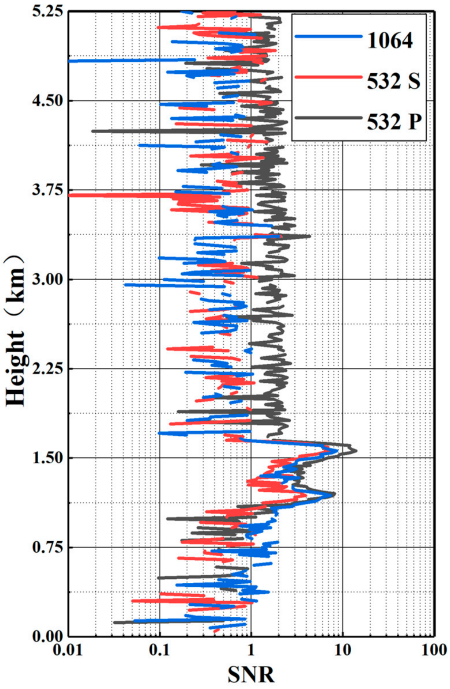

Figure 8. SNR profile at 16:00 p.m.

Figure 9a,c show the VDR and ACR of the night simulation of the spaceborne lidar input under heavy-pollution atmospheric conditions. Figure 9b,d show the simulation results of the volume depolarization ratio and the attenuated color ratio of the spaceborne lidar at night. It can be seen from the figure that, since the received signal measured by the spaceborne lidar was weak, the VDR and ACR of the simulation inversion had some noise interference compared with the ground-based lidar signal input, but the pollution aerosol can still be well distinguished.

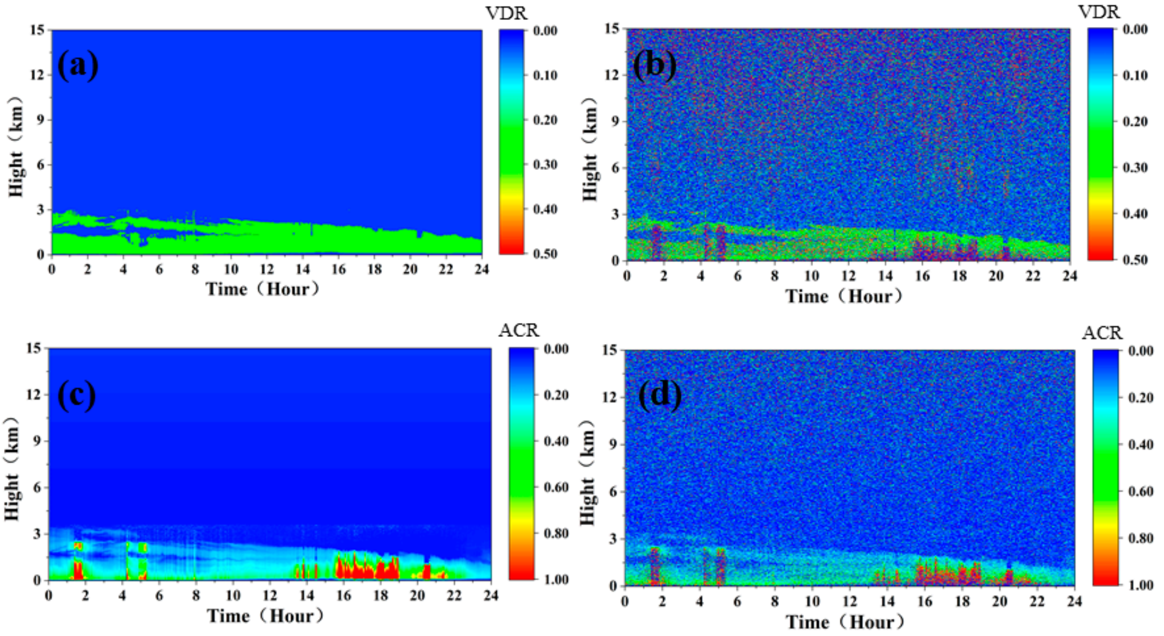

Figure 9. (**a**,**c**) VDR and ACR simulation values' input (without noise and background radiation). (**b**,**d**) The simulated results of VDR (**a**) and ACR (**b**) of spaceborne lidar at night (with noise and background radiation).

3.1.2. Observation Model in Daytime

Due to the influence of strong solar background radiation, the vertical resolution of 15 m and the cumulative pulse number of 1000 cannot meet the needs of detection. To reduce the impact of background radiation, it was found that, when the vertical resolution was 120 m and the cumulative pulse number was 10,000, the detection needs can be initially met. Figure 10a–c show the simulated measured signals at the 532 nm P, 532 nm S, and 1064 nm channels, respectively, of the spaceborne lidar (assuming that the sky background radiation intensity is a constant $Pb_{532} = 0.2\ \mathrm{W{\cdot}m^{-2}{\cdot}sr^{-1}{\cdot}nm^{-1}}$, and $Pb_{1064} = 0.08\ \mathrm{W{\cdot}m^{-2}{\cdot}sr^{-1}{\cdot}nm^{-1}}$, which do not change with time).

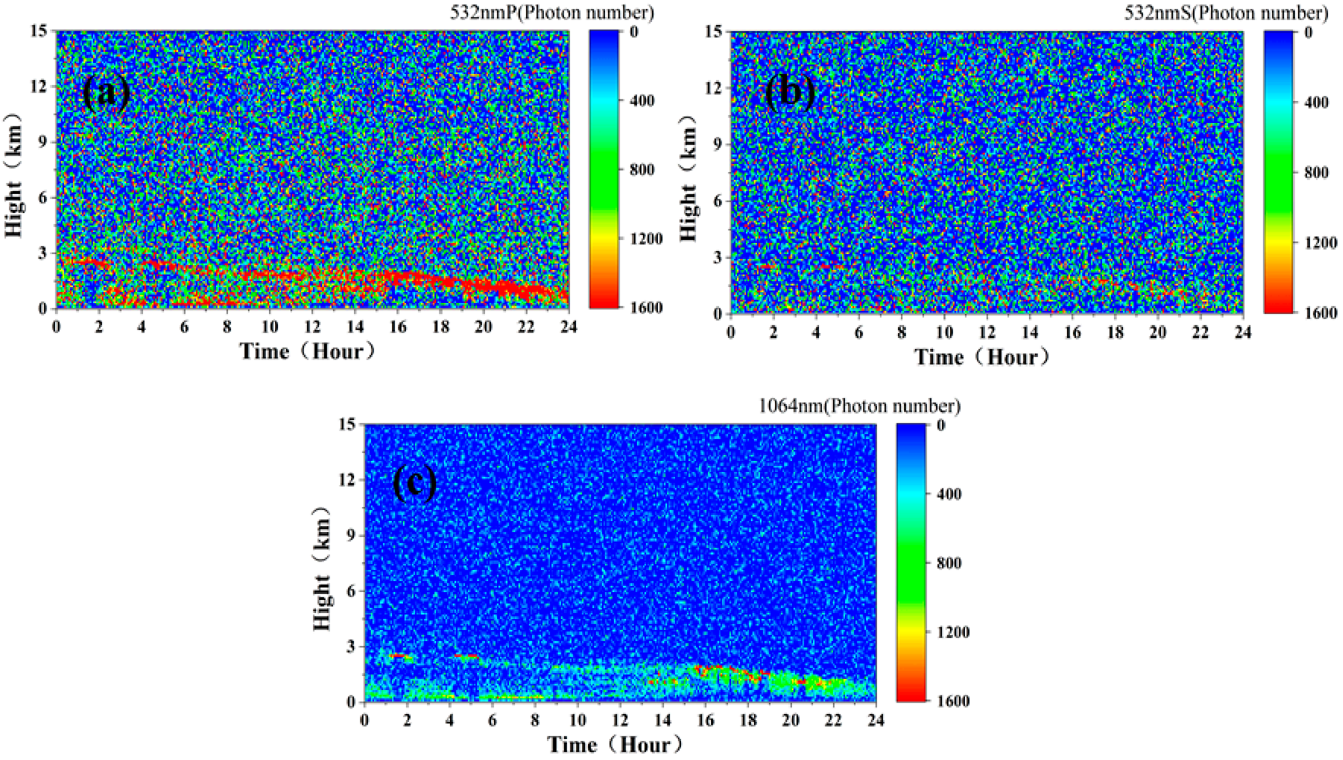

Figure 10. Simulated measured signals at 532 nm P (**a**), 532 nm S (**b**), and 1064 nm (**c**) channels of spaceborne lidar in daytime.

As can be seen from the figure, due to the influence of strong background radiation during the day, there were many noise points in the simulated signals of the three channels. In addition, the reduction of temporal and spatial resolution made some details of the aerosols and clouds missing. In general, the 532 nm P and 1064 nm channels could easily identify high-concentration clouds and aerosol layers, while the 532 nm S channel had a limited recognition effect due to low energy. As shown in Figure 11a–c, compared with the SNR of night signals, the SNR of aerosol in the daytime was around 5, except that the SNRs of clouds in the 532 nm P and 1064 nm channels were close to 10, while the SNR of only clouds in the 532 nm channel was barely between 2 and 3.

Figure 12 shows the simulation results of the VDR and ACR under this atmospheric condition. As can be seen from the figure, due to the weak echo signal of 532 S and the poor SNR, the volume depolarization ratio was small as a whole, and the aerosol layer can only be barely distinguished, while the cloud layer and the high-pollution aerosol layer can be clearly distinguished by the attenuated color ratio.

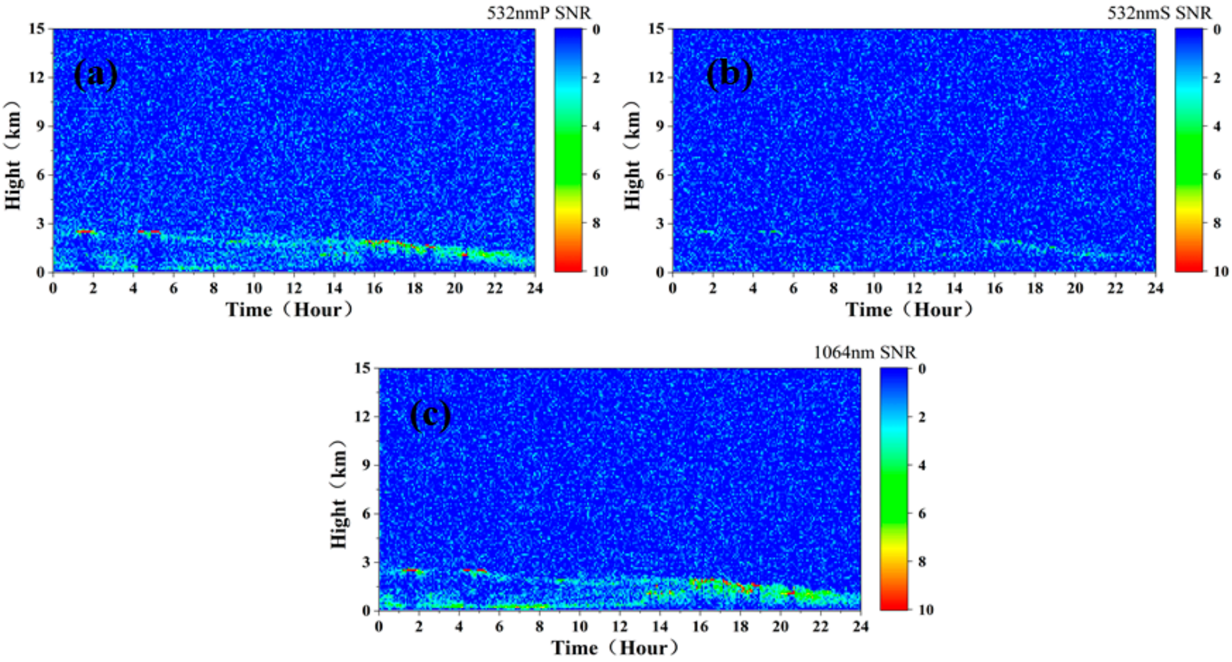

Figure 11. The simulated SNR of 532 P (**a**), 532 S (**b**), and 1064 (**c**) channels of spaceborne lidar in daytime.

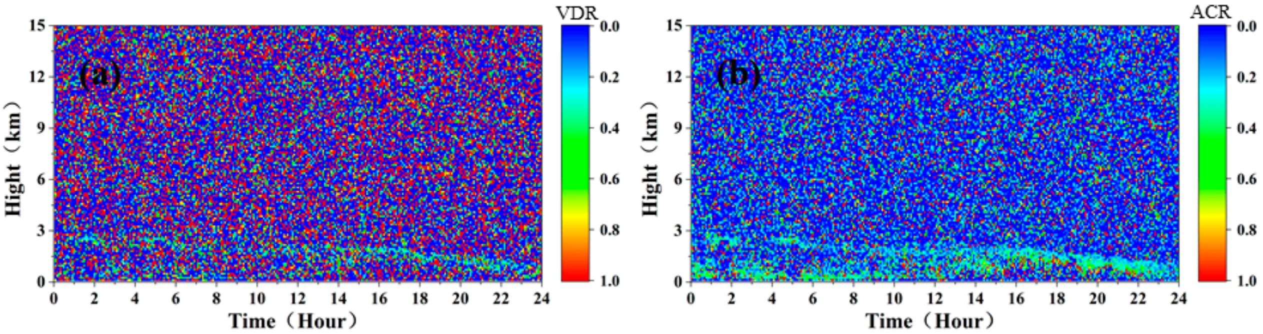

Figure 12. The simulated results of VDR (**a**) and ACR (**b**) of spaceborne lidar in daytime.

3.2. Simulation of Moderate-Pollution and High-Cloud Atmosphere

Figure 13 shows the spatial and temporal distribution characteristics of the atmospheric aerosol and cloud particle optical parameters in the moderate-pollution and high-cloud atmosphere in Hefei, China, on 22 March 2022. Figure 13a shows the aerosol extinction coefficient measured by the Mie scattering lidar at 532 nm, and Figure 13b shows the aerosol extinction coefficient of the 1064 nm simulated and retrieved with the 532 nm signal. In this atmospheric condition, the boundary layer height was nearly 2 km. The aerosol extinction coefficient inversed by a 532 nm wavelength was from 0.5~0.8 km^{-1}, and the atmospheric visibility was around 10 km. During the time from 12:00 p.m. to 18:00 p.m., there was a high concentration of aerosol pollution within the range of 0 to 2 km. During 18:00 p.m.~24:00 p.m., there were two layers of clouds at the height of 6~9 km, whose extinction coefficients were similar to those of the ground aerosol. The corresponding aerosol extinction coefficient of the 1064 nm wavelength was slightly smaller than that of 532 nm, while the cloud extinction coefficient had little change.

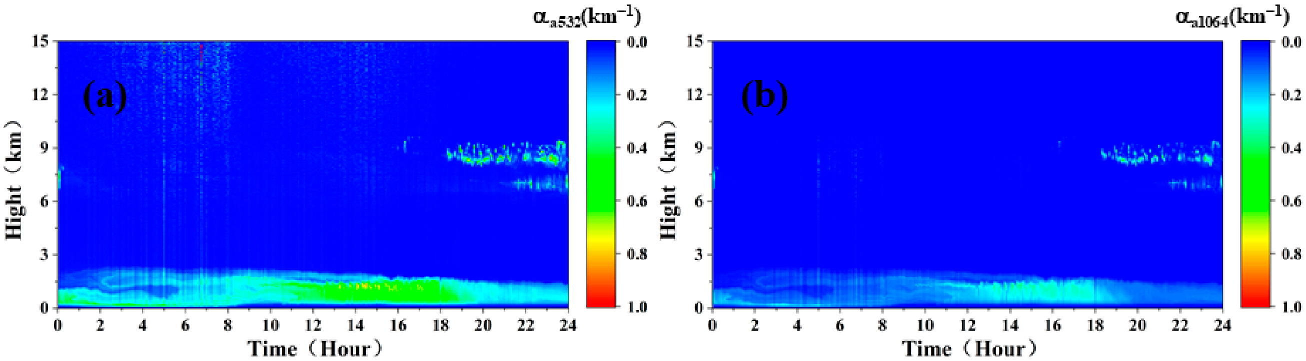

Figure 13. Aerosol extinction coefficient at 532 nm (**a**) and 1064 nm (**b**) wavelengths.

Figure 14 shows the profile of the aerosol extinction coefficient at 16:00 p.m. It can be seen from the figure that the pollution aerosols were mainly concentrated below 1.8 km at that time, and the extinction coefficient of aerosol at 532 nm was around 0.5 km^{-1}. The atmosphere above 1.8 km was very clean, basically consistent with the molecular extinction coefficient profile.

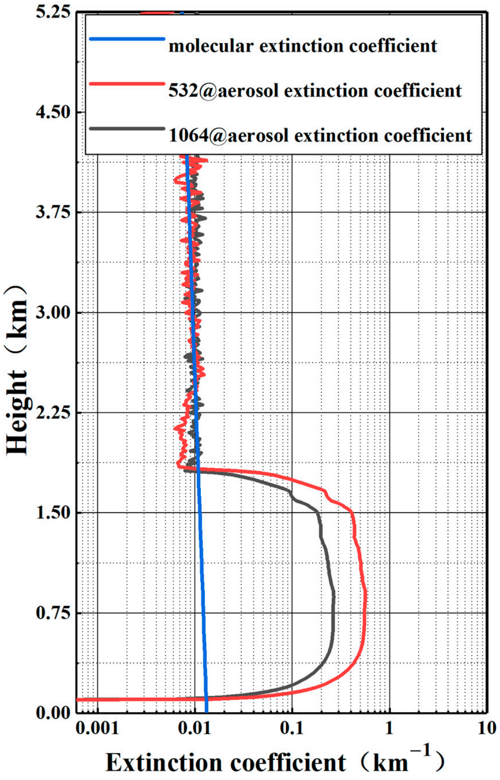

Figure 14. Atmospheric extinction coefficient at 16:00 p.m. (532 nm is from ground-based measurement, and 1064 nm is simulated for ground-based.)

3.2.1. Observation Model at Night

Figure 15 shows the spaceborne lidar simulation measurement signals under observation mode at night in the moderately polluted atmosphere. As can be seen from the simulation results at night in Figure 15, 1000 laser pulses of 532 nm and 1064 nm in the atmospheric boundary layer under moderately polluted atmospheric conditions can measure 10–15 photons in the 532 nm P channel, 5–10 photons in the 532 nm S channel, and 5–10 photons in the 1064 nm channel. For high-cloud particles with a height range of 6~9 km, the photon number measured by the three channels was basically equivalent to that of high-concentration aerosol particles in the atmospheric boundary layer.

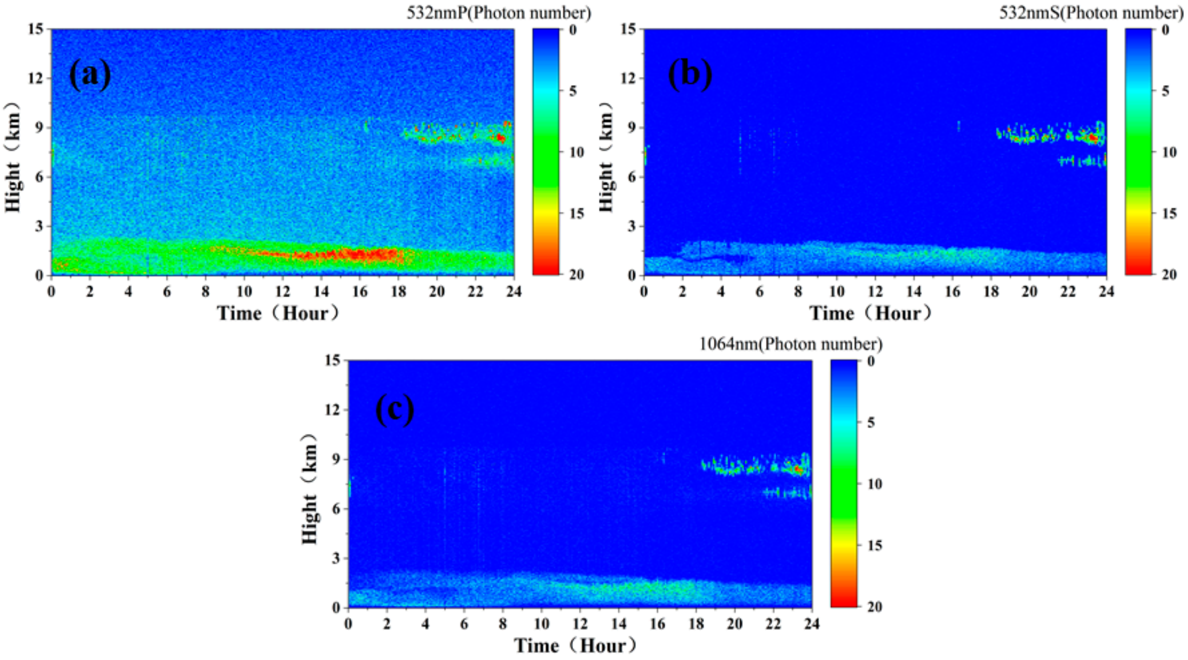

Figure 15. The simulated signal intensity of 532 P (**a**), 532 S (**b**), and 1064 (**c**) channels of spaceborne lidar.

Figure 16 shows the SNR of the 532 nm P, 532 nm S, and 1064 nm channels' simulated measured photons by the spaceborne lidar at night under moderately polluted atmospheric conditions. In the atmospheric boundary layer under moderate-pollution conditions, the SNR of the 532 nm P channel was about 5, and those of the 532 nm S and 1064 nm channels were between 2 and 5. The SNR of 6~9 km clouds was slightly higher than that of aerosol particles in the atmospheric boundary layer. At the same time, it can be seen that, although the SNR of the 532 nm channel and the 1064 nm channel were lower than that of the 532 nm P channel, their recognition of aerosol and cloud particles in the atmospheric boundary layer was higher than that of the 532 nm P channel.

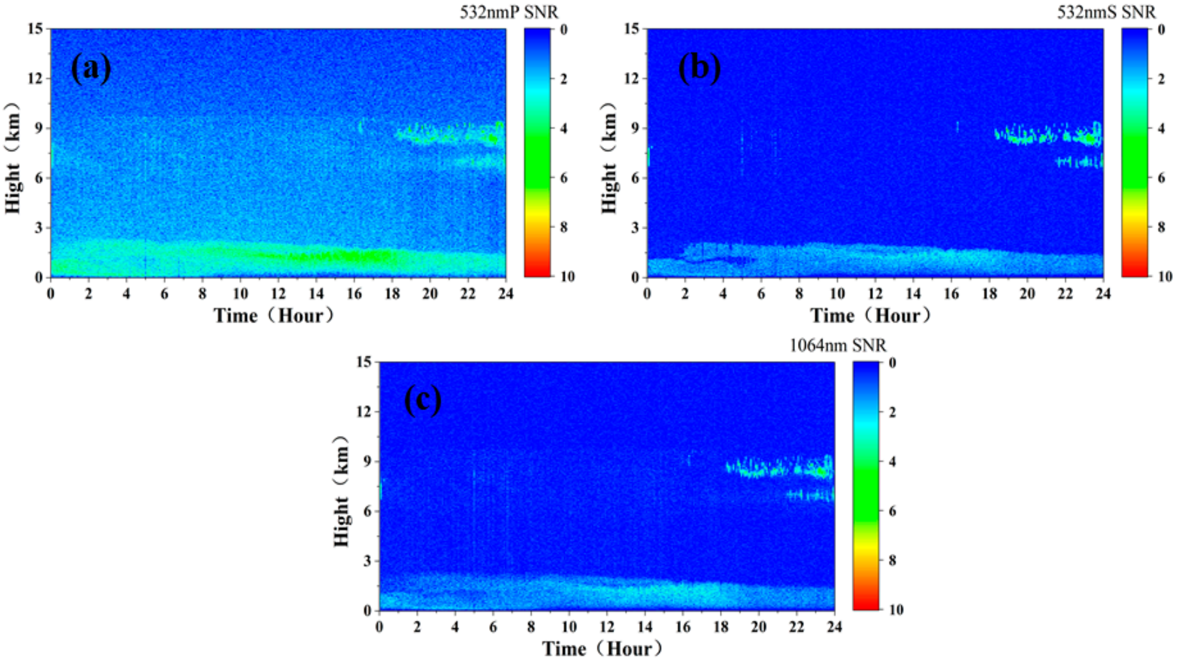

Figure 16. The simulated SNR of 532 P (**a**), 532 S (**b**), and 1064 (**c**) channels of spaceborne lidar at night.

Figure 17 shows the SNR profile at 16:00 p.m. The SNR of the 532 nm P signal in the polluted area was near 4.

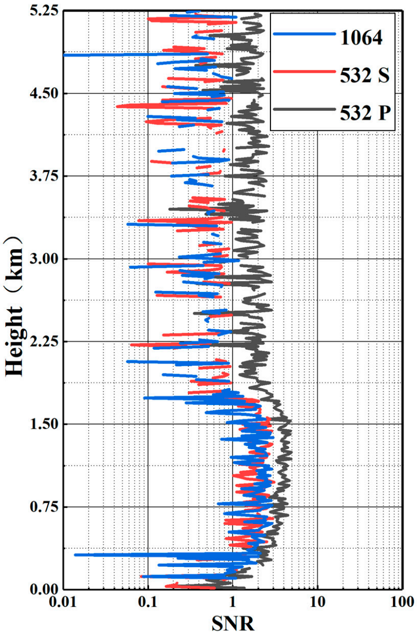

Figure 17. SNR profile at 16:00 p.m.

Figure 18 shows the simulation results of the VDR and ACR of the spaceborne lidar at night under moderately polluted atmospheric conditions. For comparison verification, the figures of the VDR and ACR of the simulation input are also given. As can be seen from the figure, compared with the VDR and ACR of the ground-based measurement, the spaceborne simulation data had obvious noise points, but it can still distinguish the aerosol and high-cloud particles in the atmospheric boundary layer well, especially the cloud layer with a good identification of 6~9 km.

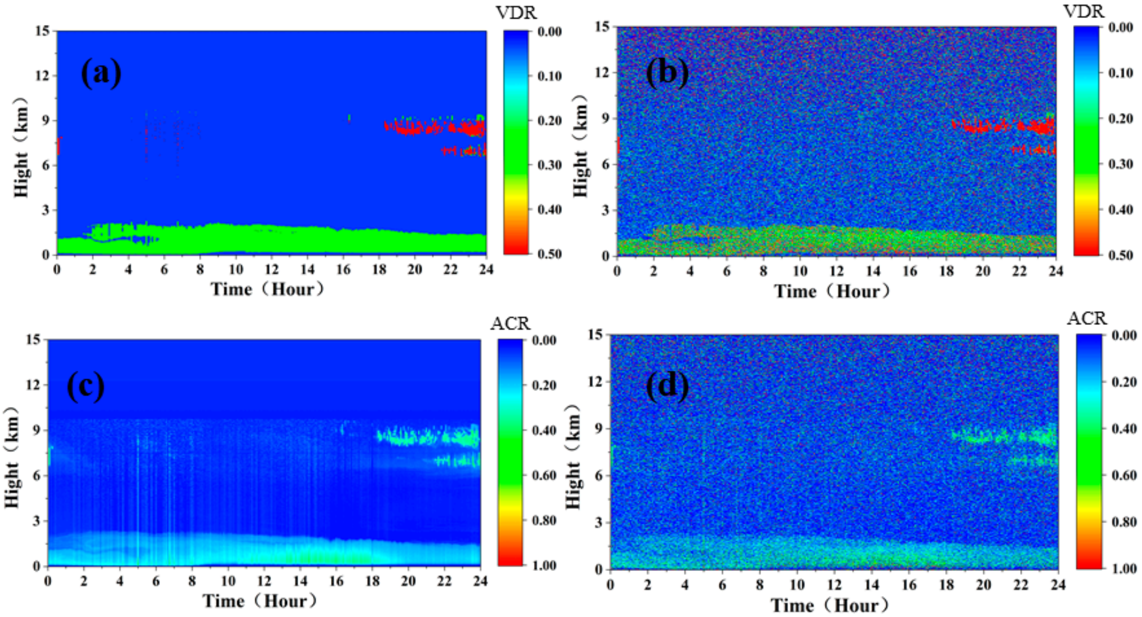

Figure 18. (**a**,**c**) VDR and ACR simulation values' input (without noise and background radiation). (**b**,**d**) The simulated results of the VDR (**a**) and ACR (**b**) of spaceborne lidar at night (with noise and background radiation).

3.2.2. Observation Model in Daytime

Figure 19 shows the spaceborne lidar simulation measurement signal in daytime observation mode under moderate pollution atmospheric conditions. As can be seen from the figure, compared with the observation at night, due to the influence of strong background light radiation during the day, the simulated measurement signals of the three channels of the spaceborne lidar all had larger noise points, and the signals of the 532 nm P and 1064 nm channels of the spaceborne lidar can identify clouds and the high-concentration aerosol layer, but failed to identify the smaller aerosol layer. The 532 nm S channel recognized only clouds, not the aerosol layer.

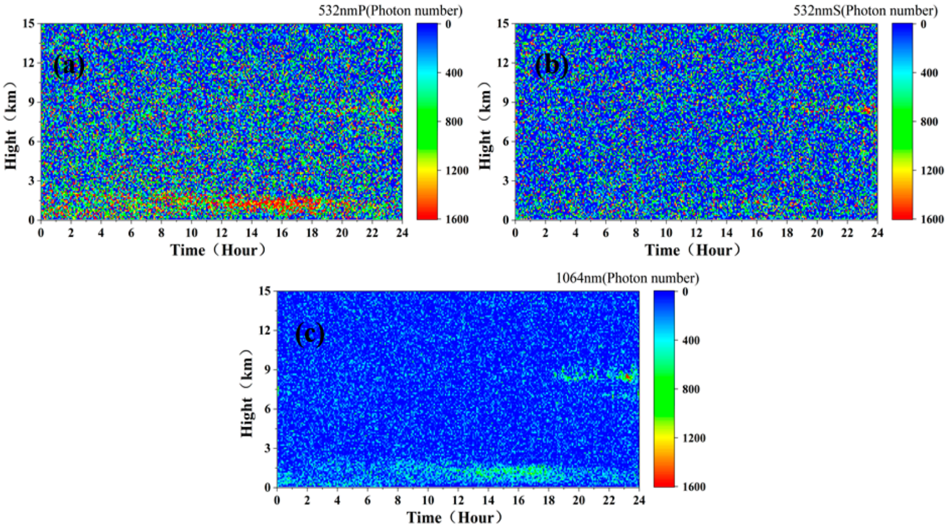

Figure 19. Simulated measured signals at 532 nm P (**a**), 532 nm S (**b**), and 1064 nm (**c**) channels of spaceborne lidar in daytime.

Figure 20 shows the SNR of the three measurement channels of the spaceborne lidar in the daytime under moderately polluted atmosphere. It can be seen from the figure that, compared with the SNR of heavy pollution in the daytime, the SNR of the three channels was smaller, about 2~3. The SNR measured at 532 nm P and 1064 nm can identify the high-concentration aerosol in the atmospheric boundary layer between 9:00 a.m. and 20:00 p.m. and the clouds at 6 to 9 km, while 532 nm S can only identify clouds.

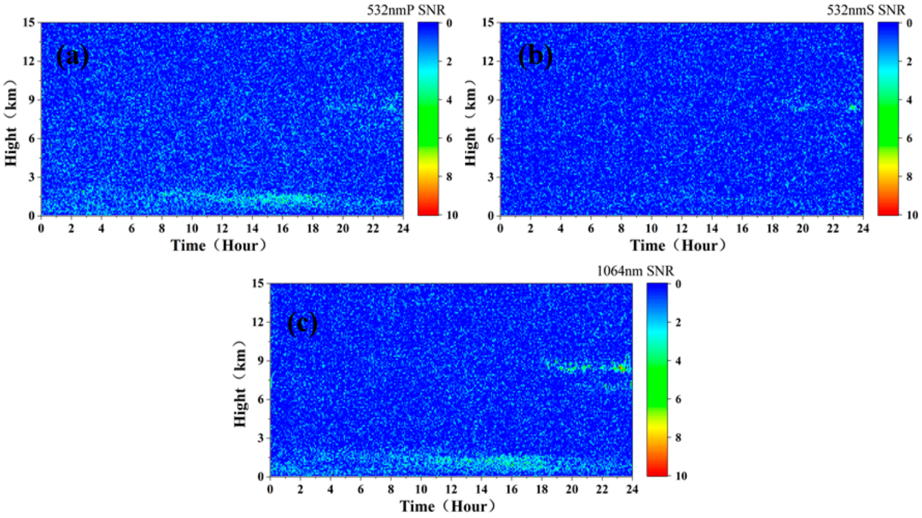

Figure 20. The simulated SNR of 532 P (**a**), 532 S (**b**), and 1064 (**c**) channels of spaceborne lidar in daytime.

Figure 21 shows the simulation results of the VDR and ACR of the spaceborne lidar in the daytime under moderate-pollution atmospheric conditions. As can be seen from the figure, under daytime conditions, the ACR can barely distinguish high-concentration aerosol particles and altostratus particles in the atmospheric boundary layer at noon, while the VDR can hardly be identified, which is mainly due to the poor SNR of the 532 nm S channel in the daytime.

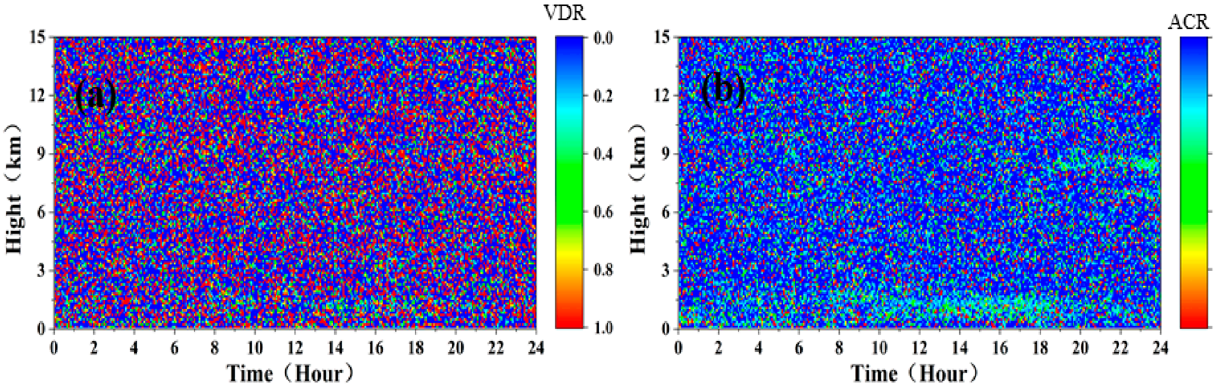

Figure 21. The simulated results of VDR (**a**) and ACR (**b**) of spaceborne lidar in daytime.

3.3. Simulation of a Clear and Cloudy Day

Figure 22 shows the spatial and temporal distribution characteristics of the atmospheric aerosol and cloud particle optical parameters on a clear and cloudy day in Hefei, China, on 28 May 2022. Figure 22a shows the aerosol extinction coefficient measured by the Mie scattering lidar at 532 nm, and Figure 22b shows the aerosol extinction coefficient of 1064 nm simulated and retrieved with the 532 nm signal. As can be seen from the figure, the ground-based lidar signal was strong, extending to an altitude of 15 km, due to the low concentration of pollution aerosol particles near the ground on that day. At the same time, high clouds existed at a height of 8~10 km from 00:00 a.m. to 12:00 p.m. and gradually decreased to a height of 2~6 km after 12:00 p.m.

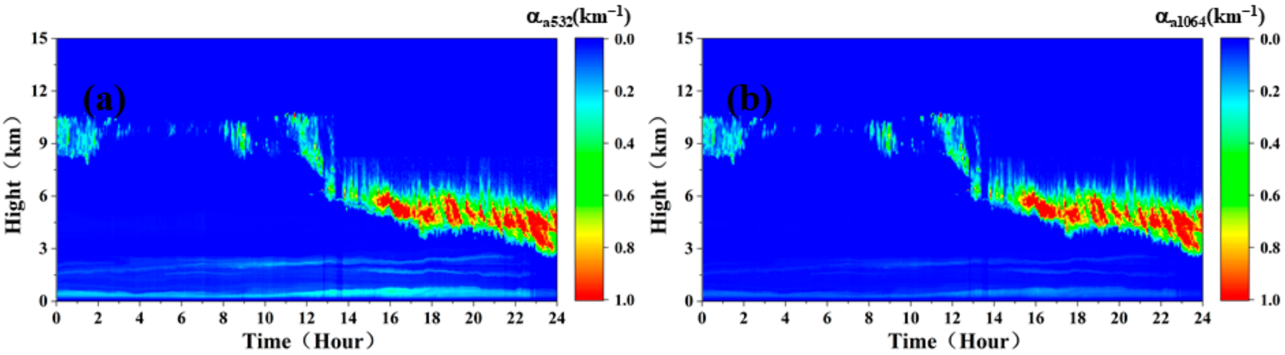

Figure 22. Aerosol extinction coefficient at 532 nm (**a**) and 1064 nm (**b**) wavelength.

Due to the low concentration of aerosol pollution near the surface on this day, there was no obvious atmospheric boundary layer. The extinction coefficient of aerosol at the 532 nm wavelength near the surface obtained by inversion was below 0.2 km^{-1}, and the corresponding visibility was above 20 km. A small amount of aerosol transport layer existed in the height range of 1.5~3 km. Correspondingly, the extinction coefficient and backscattering coefficient of 1064 nm aerosol were also very small.

For high clouds above 8 km before 12:00 p.m., the extinction coefficient of 532 nm was below 0.5 km^{-1}, while for low clouds between 2 and 6 km after 12:00 p.m., the extinction coefficients of 532 nm obtained by inversion were all greater than 1 km^{-1}, and the extinction coefficient of cloud particles with a corresponding wavelength of 1064 nm was also significantly greater than that of aerosol particles near the ground.

Figure 23 shows the profile of the aerosol extinction coefficient at 16:00 p.m. Taking the 532 nm signal as an example, the atmosphere below 3.75 km was very clean, and the extinction coefficient was no more than 0.25 km^{-1}, which is basically within 0.1 km^{-1}. There were clouds in the height range of 3.75–7.5 km, where the extinction coefficient was larger.

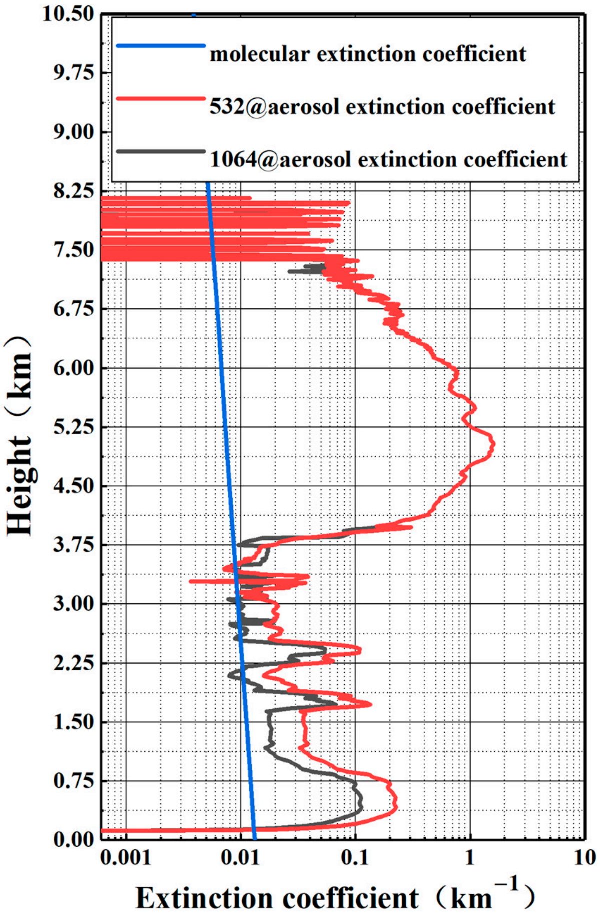

Figure 23. Atmospheric extinction coefficient at 16:00 p.m. (532 nm is from ground-based measurement, and 1064 nm is simulated for ground-based.)

3.3.1. Observation Model at Night

Figure 24 shows the spaceborne lidar simulation measurement signals under good atmospheric conditions and night observation mode. As can be seen from the figure, in clean and cloudy atmospheric conditions, due to the low concentration of aerosol in the atmospheric boundary layer, there was almost no photon number measured in the other two channels with 1000 pulses, except for the 532 nm P measurement channel, which can measure about 10 photons. However, for clouds in the height range of 3~11 km, all three channels can obtain more than 20 photons.

Figure 25 shows the SNR of the spaceborne lidar simulations at night at 532 nm P, 532 nm S, and 1064 nm under clean and cloudy atmospheric conditions. It can be seen that, in the atmospheric boundary layer under this atmospheric condition, the SNR of the 532 nm P channel's measured signal was about 2~3, while the SNR of the cloud layer was above 5. The SNR of the 532 nm S and 1064 nm channels was almost 1 for the aerosol in the atmospheric boundary layer, while the SNR was above 5 for clouds.

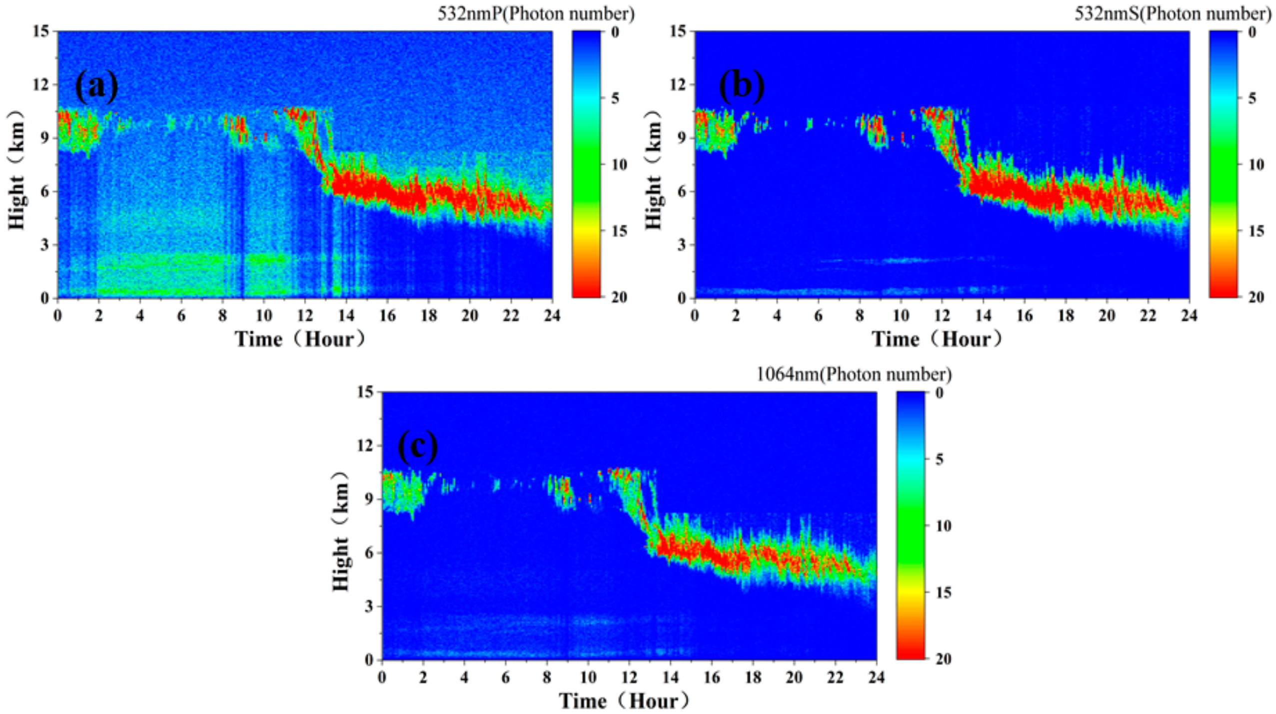

Figure 24. The simulated signal intensity of 532 P (**a**), 532 S (**b**), and 1064 (**c**) channels of spaceborne lidar.

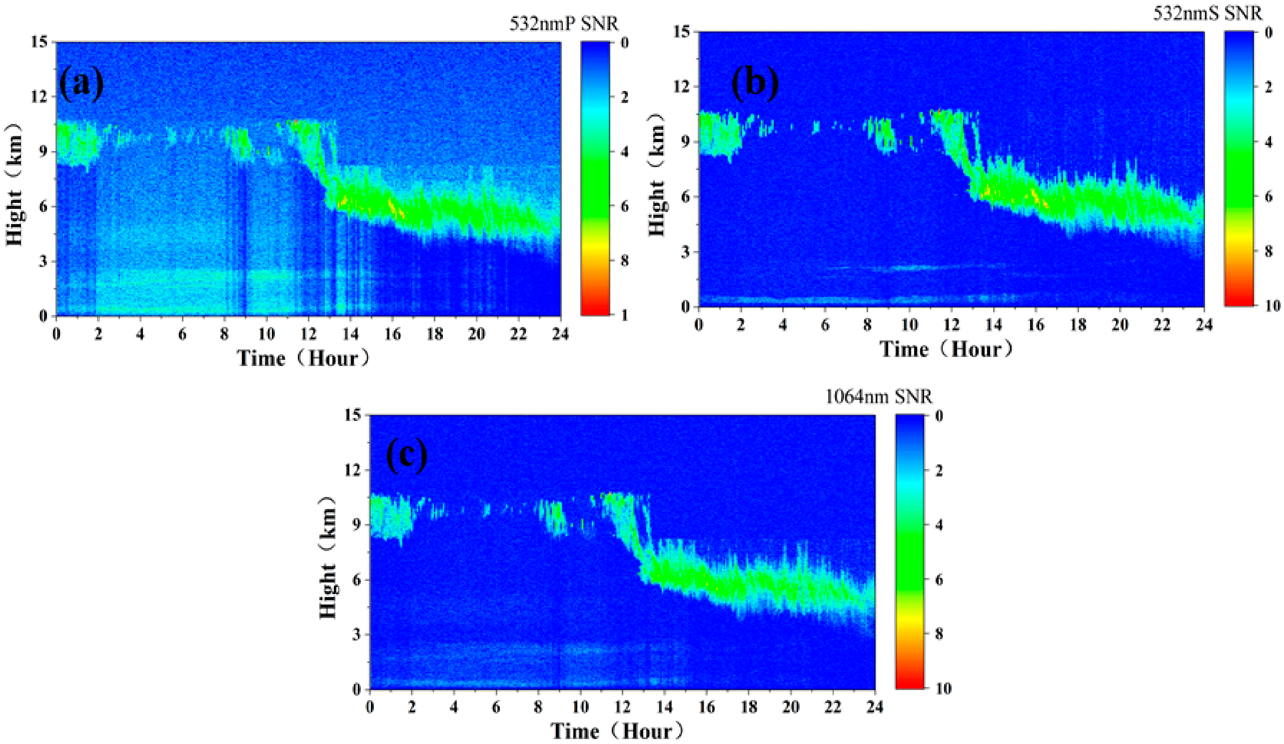

Figure 25. The simulated SNR of 532 P (**a**), 532 S (**b**), and 1064 (**c**) channels of spaceborne lidar at night.

Figure 26 shows the SNR profile at 16:00 p.m. The SNR was near 4 within a 4.5–7.5 km altitude range. In the area below 4.5 km, the SNR was poor due to the low aerosol content.

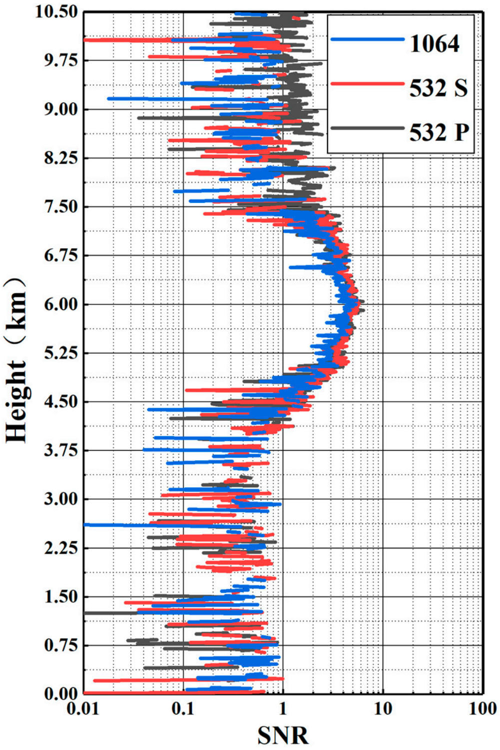

Figure 26. SNR profile at 16:00 p.m.

Figure 27b,d show the simulation results of the spaceborne lidar VDR and ACR at night under fine cloudy atmospheric conditions. For comparison and verification, the VDR and ACR of the input of the simulation are also given in Figure 27a,c. It can be seen from the figure that only clouds can be identified by the spaceborne simulation VDR and ACR, while the aerosol in the boundary layer cannot be identified.

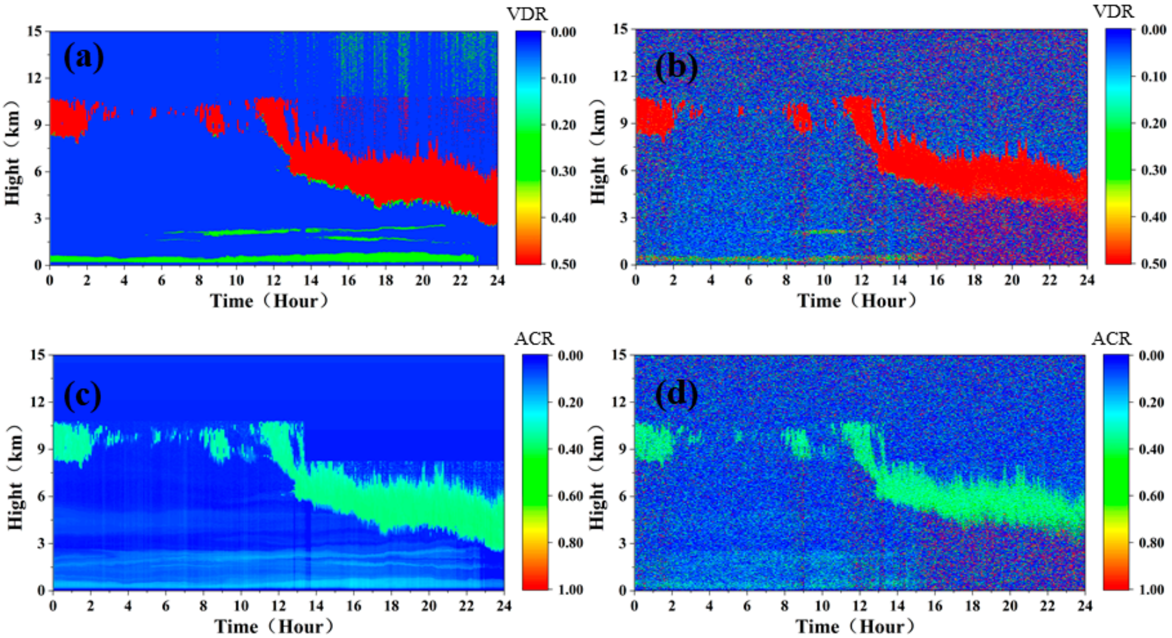

Figure 27. (**a**,**c**) VDR and ACR simulation values input (without noise and background radiation). (**b**,**d**) The simulated results of VDR (**a**) and ACR (**b**) of spaceborne lidar at night (with noise and background radiation).

3.3.2. Observation Model in Daytime

Figure 28 shows the spaceborne lidar simulation measurement signal in clean and cloudy atmosphere and daytime observation mode. As can be seen from the figure, compared with night observation, due to the influence of strong background light radiation during the day, the simulated measurement signals of the three channels all have larger noise points, and due to the reduction of time and spatial resolution, the spatiotemporal details of aerosol and cloud became worse. All three measurement channels can be used to identify clouds relatively, while small aerosol layers cannot be identified.

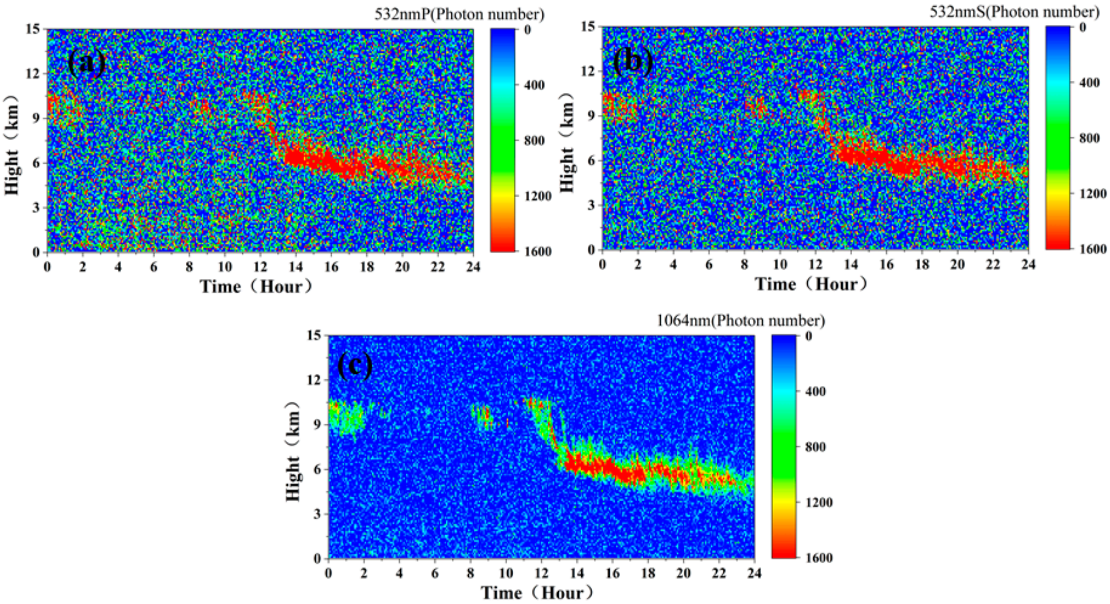

Figure 28. Simulated measured signals at 532 nm P (**a**), 532 nm S (**b**), and 1064 nm (**c**) channels of spaceborne lidar in daytime.

Figure 29 shows the SNR of the three measurement channels of the spaceborne lidar in the daytime under a clean and cloudy atmosphere. It can be seen from the figure that the three channels all had an SNR of more than 5 for clouds, and the 1064 nm measurement channel had an SNR of more than 10.

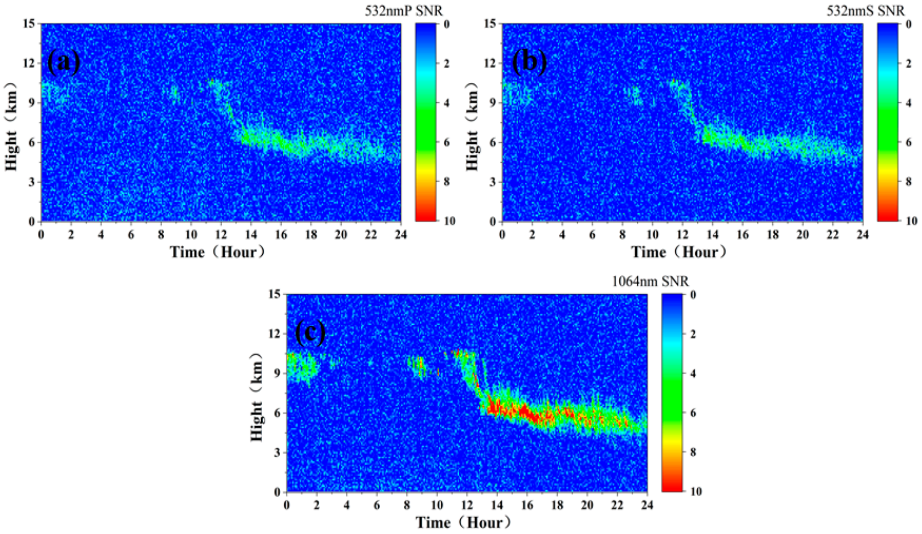

Figure 29. The simulated SNR of 532 P (**a**), 532 S (**b**), and 1064 (**c**) channels of spaceborne lidar in daytime.

Figure 30 shows the simulation results of the VDR and ACR of the spaceborne lidar in the daytime under clean and cloudy atmospheric conditions. As can be seen from the figure, under daytime conditions, clouds with a height range of 3~10 km can be well identified according to the VDR and ACR.

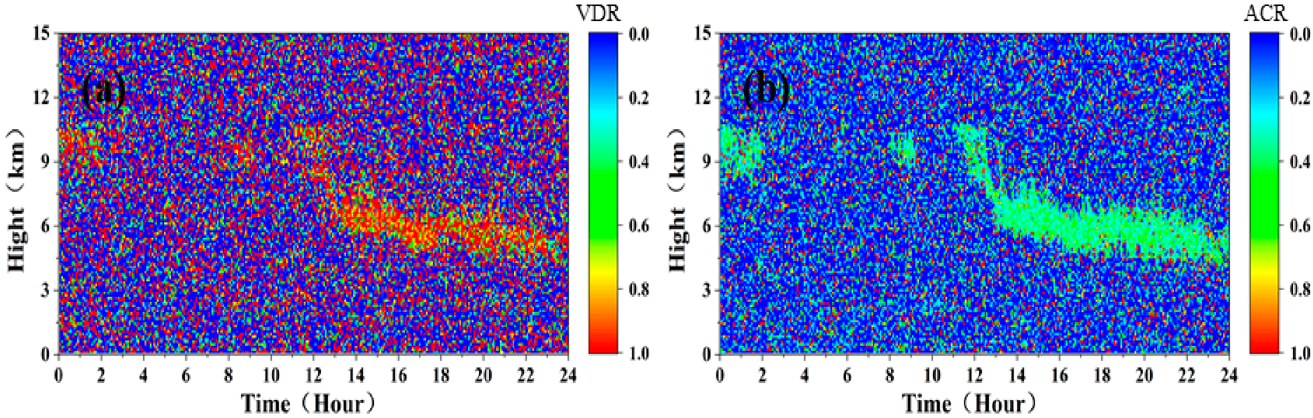

Figure 30. The simulated results of VDR (**a**) and ACR (**b**) of spaceborne lidar in daytime.

4. Conclusions

In this paper, the detection performance of the spaceborne lidar system was preliminarily evaluated by simulation. The photon number, SNR, VDR, and ACR of the spaceborne lidar detection signals were simulated, and the factors affecting the detection performance of the system were summarized. The results showed that solar background radiation had the greatest influence on the SNR. When the cumulative pulse number was 1000 and the vertical separation rate was 15 m for night detection, the detection needs can be fully met, and the clouds and aerosol layers with an extinction coefficient above 0.3 km^{-1} at 532 nm can be accurately identified. In daytime detection, due to background light intensity, the detection SNR was improved by sacrificing the temporal and spatial resolution. When the cumulative pulse number was 10,000 and the vertical resolution was 120 m, the heavy-pollution aerosol layer and the thick cloud can be well identified. For moderate pollution, only partial aerosol and cloud identification can be achieved. On clean days, it was impossible to find exactly where the boundary layer is. In the following work, the satellite tool kit (STK) and radiation transfer model should be combined with the satellite orbit to simulate more real solar background radiation.

Author Contributions: Supervision, conceptualization, funding acquisition, C.X.; methodology, resources, K.X., J.C.; software, B.W., L.C.; data curation, X.D.; writing—original draft preparation, J.J.; writing—review and editing, J.J. All authors have read and agreed to the published version of the manuscript.

Funding: This work was supported in part by the Civil Aerospace Technology Pre-research Project (D040103), the Strategic Priority Research Program of the Chinese Academy of Sciences (XDA17040524), the Anhui Province 2017 High-level Science and Technology Talent Team Project (010567900), and the Key Program of 13th Five-Year Plan, CASHIPS (KP-2019-05).

Data Availability Statement: The data presented in this study are available upon request from the corresponding author.

Acknowledgments: The authors thank Xie Chenbo of Anhui Institute of Optics and Fine Mechanics, Hefei Institutes of Physical Science, and Chinese Academy of Sciences for providing the data.

Conflicts of Interest: The authors declare no conflict of interest.

References

1. Gunaseelan, I.; Bhaskar, V. In Aerosols and Clouds Interactions in an Urban Atmosphere. In Proceedings of the 29th International Laser Radar Conference (ILRC), Hefei, China, 24–28 June 2019.
2. Eck, T.F.; Holben, B.N.; Reid, J.S.; Xian, P.; Giles, D.M.; Sinyuk, A.; Smirnov, A.; Schafer, J.S.; Slutsker, I.; Kim, J.; et al. Observations of the Interaction and Transport of Fine Mode Aerosols with Cloud and/or Fog in Northeast Asia from Aerosol Robotic Network and Satellite Remote Sensing. *J. Geophys. Res.-Atmos.* **2018**, *123*, 5560–5587. [CrossRef]
3. Brooks, S.D.; Thornton, D.C.O. Marine Aerosols and Clouds. In *Annual Review of Marine Science*; Carlson, C.A., Giovannoni, S.J., Eds.; Annual Reviews: San Mateo, CA, USA, 2018; Volume 10, pp. 289–313.
4. Seinfeld, J.H.; Bretherton, C.; Carslaw, K.S.; Coe, H.; DeMott, P.J.; Dunlea, E.J.; Feingold, G.; Ghan, S.; Guenther, A.B.; Kahn, R.; et al. Improving our fundamental understanding of the role of aerosol-cloud interactions in the climate system. *Proc. Natl. Acad. Sci. USA* **2016**, *113*, 5781–5790. [CrossRef]
5. Wang, Y.J.; Sun, L.; Liu, D.; Wang, Z.; Wang, Z.Z.; Xie, C.B. In Cloud and Aerosol Interaction Observed in Skynet Hefei Site in China. In Proceedings of the 27th International Laser Radar Conference (ILRC), New York, NY, USA, 5–10 July 2015; Natl Ocean & Atmospher Adm, Cooperat Remote Sensing Sci & Technol Ctr.: New York, NY, USA, 2015.
6. Kay, J.E.; L'Ecuyer, T.; Chepfer, H.; Loeb, N.; Morrison, A.; Cesana, G. Recent Advances in Arctic Cloud and Climate Research. *Curr. Clim. Chang. Rep.* **2016**, *2*, 159–169. [CrossRef]
7. Belikov, Y.E.; Dyshlevsky, S.V.; Repin, A.Y. Effect of Thin High Clouds and Aerosol Layers on the Heating and Dissipation of Low-level Clouds in the Arctic. *Russ. Meteorol. Hydrol.* **2021**, *46*, 245–255. [CrossRef]
8. Hartmann, D.L. Tropical anvil clouds and climate sensitivity. *Proc. Natl. Acad. Sci. USA* **2016**, *113*, 8897–8899. [CrossRef]
9. Scott, C.E.; Arnold, S.R.; Monks, S.A.; Asmi, A.; Paasonen, P.; Spracklen, D.V. Substantial large-scale feedbacks between natural aerosols and climate. *Nat. Geosci.* **2018**, *11*, 44. [CrossRef]
10. Schafer, B.; Carlsen, T.; Hanssen, I.; Gausa, M.; Storelvmo, T. Observations of cold-cloud properties in the Norwegian Arctic using ground-based and spaceborne lidar. *Atmos. Chem. Phys.* **2022**, *22*, 9537–9551. [CrossRef]
11. Dionisi, D.; Brando, V.E.; Volpe, G.; Colella, S.; Santoleri, R. Seasonal distributions of ocean particulate optical properties from spaceborne lidar measurements in Mediterranean and Black sea. *Remote Sens. Environ.* **2020**, *247*, 111889. [CrossRef]
12. Gupta, G.; Ratnam, M.V.; Madhavan, B.L.; Prasad, P.; Narayanamurthy, C.S. Vertical and spatial distribution of elevated aerosol layers obtained using long-term ground-based and space-borne lidar observations. *Atmos. Environ.* **2021**, *246*, 118172. [CrossRef]
13. Chanin, M.L.; Hauchecorne, A.; Malique, C.; Nedeljkovic, D.; Blamont, J.E.; Desbois, M.; Tulinov, G.; Melnikov, V. First results of the ALISSA lidar on board the MIR platform. *Comptes Rendus De L'academie Des Sci. Ser. IIA Earth Planet. Sci.* **1999**, *328*, 359–366.
14. Hu, Y.X.; Vaughan, M.; Liu, Z.Y.; Lin, B.; Yang, P.; Flittner, D.; Hunt, B.; Kuehn, R.; Huang, J.P.; Wu, D.; et al. The depolarization-attenuated backscatter relation: CALIPSO lidar measurements vs. theory. *Opt. Express* **2007**, *15*, 5327–5332. [CrossRef] [PubMed]
15. Burton, S.P.; Ferrare, R.A.; Vaughan, M.A.; Omar, A.H.; Rogers, R.R.; Hostetler, C.A.; Hair, J.W. Aerosol classification from airborne HSRL and comparisons with the CALIPSO vertical feature mask. *Atmos. Meas. Tech.* **2013**, *6*, 1397–1412. [CrossRef]
16. Winker, D.M.; Hunt, W.; Hostetler, C. In Status and performance of the CALIOP lidar. In Proceedings of the Conference on Laser Radar Techniques for Atmospheric Sensing, Maspalomas, Spain, 14–16 September 2004; pp. 8–15.
17. Powell, K.A. The Development of the CALIPSO LiDAR Simulator. Master's Thesis, The College of William and Mary ProQuest Dissertations Publishing, Williamsburg, VA, USA, 2005; p. 1539626831.
18. Stoffelen, A.; Pailleux, J.; Kallen, E.; Vaughan, J.M.; Isaksen, L.; Flamant, P.; Wergen, W.; Andersson, E.; Schyberg, H.; Culoma, A.; et al. The atmospheric dynamics mission for global wind field measurement. *Bull. Am. Meteorol. Soc.* **2005**, *86*, 73. [CrossRef]
19. Winker, D.M.; Couch, R.H.; McCormick, M.P. An overview of LITE: NASA's lidar in-space technology experiment. *Proc. IEEE* **1996**, *84*, 164–180. [CrossRef]
20. Couch, R.H.; Rowland, C.W.; Ellis, K.S.; Blythe, M.P.; Regan, C.P.; Koch, M.R.; Antill, C.W.; Kitchen, W.L.; Cox, J.W.; Delorme, J.F.; et al. Lidar in-Space Technology Experiment (Lite)-Nasas 1st in-Space Lidar System for Atmospheric Research. *Opt. Eng.* **1991**, *30*, 88–95. [CrossRef]
21. Proestakis, E.; Amiridis, V.; Marinou, E.; Binietoglou, I.; Ansmann, A.; Wandinger, U.; Hofer, J.; Yorks, J.; Nowottnick, E.; Makhmudov, A.; et al. Earlinet evaluation of the CATS Level 2 aerosol backscatter coefficient product. *Atmos. Chem. Phys.* **2019**, *19*, 11743–11764. [CrossRef]
22. Pauly, R.M.; Yorks, J.E.; Hlavka, D.L.; McGill, M.J.; Amiridis, V.; Palm, S.P.; Rodier, S.D.; Vaughan, M.A.; Selmer, P.A.; Kupchock, A.W.; et al. Cloud-Aerosol Transport System (CATS) 1064 nm calibration and validation. *Atmos. Meas. Tech.* **2019**, *12*, 6241–6258. [CrossRef]
23. Sellitto, P.; Bucci, S.; Legras, B. Comparison of ISS-CATS and CALIPSO-CALIOP Characterization of High Clouds in the Tropics. *Remote Sens.* **2020**, *12*, 3946. [CrossRef]
24. Yorks, J.E.; McGill, M.J.; Palm, S.P.; Hlavka, D.L.; Selmer, P.A.; Nowottnick, E.P.; Vaughan, M.A.; Rodier, S.D.; Hart, W.D. An overview of the CATS level 1 processing algorithms and data products. *Geophys. Res. Lett.* **2016**, *43*, 4632–4639. [CrossRef]
25. Ge, J.M.; Wang, Z.Q.; Wang, C.; Yang, X.; Dong, Z.X.; Wang, M.H. Diurnal variations of global clouds observed from the CATS spaceborne lidar and their links to large-scale meteorological factors. *Clim. Dyn.* **2021**, *57*, 2637–2651. [CrossRef]
26. Mao, F.Y.; Luo, X.; Song, J.; Liang, Z.X.; Gong, W.; Chen, W.B. Simulation and retrieval for spaceborne aerosol and cloud high spectral resolution lidar of China. *Sci. China-Earth Sci.* **2022**, *65*, 570–583. [CrossRef]

27. Sasano, Y.; Browell, E.V. Light-Scattering Characteristics of Various Aerosol Types Derived from Multiple Wavelength Lidar Observations. *Appl. Opt.* **1989**, *28*, 1670–1679. [CrossRef] [PubMed]
28. Frehlich, R. Simulation of coherent Doppler lidar performance for space-based platforms. *J. Appl. Meteorol.* **2000**, *39*, 245–262. [CrossRef]
29. Liu, Z.Y.; Sugimoto, N. Simulation study for cloud detection with space lidars by use of analog detection photomultiplier tubes. *Appl. Opt.* **2002**, *41*, 1750–1759. [CrossRef]
30. Filipitsch, F.; Buras, R.; Fuchs, M. In Model Studies on the Retrieval of Aerosol Properties beneath Cirrus Clouds for a Spaceborne HSRL. In Proceedings of the International Radiation Symposium on Radiation Processes in the Atmosphere and Ocean (IRS), Berlin, Germany, 6–10 August 2012; Free Univ Berlin: Berlin, Germany, 2012; pp. 452–455.
31. Boquet, M.; Royer, P.; Cariou, J.P.; Machta, M.; Valla, M. Simulation of Doppler Lidar Measurement Range and Data Availability. *J. Atmos. Ocean. Technol.* **2016**, *33*, 977–987. [CrossRef]
32. Reverdy, M.; Chepfer, H.; Donovan, D.; Noel, V.; Cesana, G.; Hoareau, C.; Chiriaco, M.; Bastin, S. An EarthCARE/ATLID simulator to evaluate cloud description in climate models. *J. Geophys. Res.-Atmos.* **2015**, *120*, 11090–11113. [CrossRef]
33. Fernald, F.G. Analysis of Atmospheric Lidar Observations-Some Comments. *Appl. Opt.* **1984**, *23*, 652–653. [CrossRef]
34. Murayama, T.; Okamoto, H.; Kaneyasu, N.; Kamataki, H.; Miura, K. Application of lidar depolarization measurement in the atmospheric boundary layer: Effects of dust and sea-salt particles. *J. Geophys. Res.-Atmos.* **1999**, *104*, 31781–31792. [CrossRef]
35. Xie, C.B.; Zhou, J. In Method and analysis of calculating signal-to-noise ratio in lidar sensing. In Proceedings of the Conference on Optical Technologies for Atmospheric, Ocean, and Environmental Studies, Beijing, China, 18–22 October 2004; pp. 738–746.
36. Diomede, P.; Dell'Aglio, M.; Pisani, G.; De Pascale, O. In Lidar system for depolarization ratio measurements: Development and preliminary results. In Proceedings of the 12th International Workshop on Lidar Multiple Scattering Experiments, Oberpfaffenhofen, Germany, 10–12 September 2002; German Aerosp Ctr: Oberpfaffenhofen, Germany, 2002; pp. 212–218.
37. Wang, Z.Z.; Liu, D.; Zhou, J.; Wang, Y.J. Experimental determination of the calibration factor of polarization-Mie lidar. *Opt. Rev.* **2009**, *16*, 566–570. [CrossRef]
38. Tomasi, C.; Vitale, V.; Petkov, B.; Lupi, A.; Cacciari, A. Improved algorithm for calculations of Rayleigh-scattering optical depth in standard atmospheres. *Appl. Opt.* **2005**, *44*, 3320–3341. [CrossRef]
39. CALIOP Algorithm Theoretical Basis Document Calibration and Level 1 Data Products. Available online: https://www.researchgate.net/publication/238622694_Calibration_and_Level_1_Data_Products (accessed on 15 May 2023).